The effect of stress changes on time-dependent earthquake probabilities for the central Wasatch Fault Zone, Utah, USA.

Authors

A. Verdecchia[1,2], S. Carena[2], B. Pace[3] and C. B. DuRoss[4]

Affiliation

[1]Institute of Geology, Mineralogy and Geophysics, Ruhr-University Bochum, Bochum, Germany.

[2]Department of Earth and Environmental Sciences, Ludwig-Maximilians University, Munich, Germany.

[3]DiSPUTer, Universita' G. d'Annunzio di Chieti-Pescara, Chieti, Italy.

[4]U.S. Geological Survey, 1711 Illinois Street, Golden, Colorado, 80401.

Corresponding author: Alessandro Verdecchia, Institute of Geology, Mineralogy and Geophysics, Ruhr-University Bochum, Bochum, Germany.
(alessandro.verdecchia@rub.de)

Summary

Static and quasi-static Coulomb stress changes produced by large earthquakes can modify the probability of occurrence of subsequent events on neighboring faults. This approach is based on physical (Coulomb stress changes) and statistical (probability calculations) models, which are influenced by the quality and quantity of data available in the study region. Here, we focus on the Wasatch Fault Zone (WFZ), a well-studied active normal fault system having abundant geologic and paleoseismological data. Paleoseismological trench investigations of the WFZ indicate that at least 24 large, surface-faulting earthquakes have ruptured the fault's five central, 35–59-km long segments since ~7 ka. Our goal is to determine if the stress changes due to the youngest paleoevents have significantly modified the present-day probability of occurrence of large earthquakes on each of the segments. For each segment, we modeled the cumulative (coseismic + postseismic) Coulomb stress changes (ΔCFS_{cum}) due to earthquakes younger than the most recent event on the segment in question and applied the resulting values to the time-dependent probability calculations. Results from the Coulomb stress modeling suggest that the Brigham City, Salt Lake City, and Provo segments have accumulated ΔCFS_{cum} larger than 10 bars, whereas the Weber segment has experienced a stress decrease of 5 bars, in the scenario of recent rupture of the Great Salt Lake fault to the west. Probability calculations predict high probability of occurrence for the Brigham City and Salt Lake City segments, due to their long elapsed times (>1-2 ka) when compared to the Weber, Provo, and Nephi segments (< 1 ka). The range of calculated coefficients of variation (CV) has a large influence on the final probabilities, mostly in the case of the Brigham City segment. Finally, when the Coulomb stress and the probability models are combined, our results indicate that the ΔCFS_{cum} resulting from earthquakes postdating the youngest events on each of the five segments substantially affects the probability calculations for three of the segments: Brigham City, Salt Lake City, and Provo. The probability of occurrence of a large earthquake in the next 50 years on these three segments may therefore be underestimated if a time-independent approach, or a time-dependent approach that does not consider ΔCFS, is adopted.

Keywords: North America, Probabilistic forecasting, Earthquake interaction, forecasting, and prediction, Paleoseismology, Rheology: crust and lithosphere, Dynamics and mechanics of faulting.

1. Introduction

Physical models based on Coulomb stress changes (ΔCFS) have been implemented in statistical probabilistic fault-based seismic hazard models for different regions such as Japan, Turkey, California, and Italy (*Toda et al.*, 1998; *Stein*, 1999; *Parsons*, 2005; *Console et al.*, 2008; *Pace et al.*, 2014). Not surprisingly, these regions, when compared to other tectonically active areas, are characterized by the existence of abundant data on large historical, instrumental, and paleoseismological earthquakes. This is necessary because the results from this kind of approach are often subject to large uncertainties associated with the quantity and quality of input parameters such as slip rate, mean recurrence, and elapsed time since the most recent earthquake.

The Wasatch Fault Zone (WFZ)—a normal fault zone located at the eastern boundary of the Basin and Range province (Figure 1)—has been the focus of at least 25 published paleoseismological investigations in the last ~20 years (*Personius et al.*, 2012), and at least 24 large, surface-faulting earthquakes have been detected on its five main central segments (*DuRoss et al.*, 2016). In addition, several geodetic studies (*Friedrich et al.*, 2003; *Chang et al.*, 2006; *Hammond et al.*, 2009) have shown that, despite the absence of large historical earthquakes, the WFZ is characterized by higher deformation rates (~2 mm/yr) than the central and western Basin and Range, and it therefore is a hazard for the ~2 million people living along the Wasatch Front. Therefore, the WFZ is an ideal study region for time-dependent probabilistic seismic hazard analysis.

Despite the abundant and high-quality paleoseismological data for the WFZ, earthquake-probability studies of the fault have not considered the degree to which the history of past surface-faulting earthquakes has modified the stress accumulated on the fault, and the resulting effect on time-dependent earthquake probabilities. *McCalpin and Nishenko* (1996) first adopted a purely time-dependent approach to calculating the probability of future large earthquakes on the five central segments of the WFZ. These authors estimated high probabilities (> 10%) of M ≥ 7 earthquakes on the Brigham City and Salt Lake City segments (Figure 1) for the next 50 and 100 years, and relatively low probabilities (< 5%) on the other three segments (the Weber, Provo, and Nephi segments; Figure 1), which have more recently experienced large earthquakes. *McCalpin & Nishenko* (1996) did not consider paleoseismological earthquakes as sources of stress changes. Later, *Chang & Smith* (2002) introduced the effect of stress changes on probabilistic seismic hazard analysis of the Salt Lake City segment of the central WFZ. However, *Chang & Smith* (2002) only considered the effect of possible future events on adjacent segments (Weber and Provo), rather than stress changes due to past earthquakes. Recently, the Working Group on Utah Earthquake Probabilities (WGUEP) produced a detailed study (*WGUEP*, 2016) concerning the probabilistic earthquake forecasts for the Wasatch Front region. By combining a time-dependent and a time-independent approach for the five central segments of the WFZ, the authors calculated the highest probability on the Salt Lake City segment (5.8%) of one or more M ≥ 6.75 earthquakes in the next 50 years), and a total probability of 18% (again of one or more M ≥ 6.75 earthquakes in the next 50 years) along the entire WFZ. The WGUEP (2016) study did not include fault interactions through Coulomb stress changes in the calculations.

Here, we evaluate the influence of stress changes due to past earthquakes on a probabilistic seismic hazard model for the central WFZ. We first compute the probability of single-segment earthquakes occurring on the Brigham City, Weber, Salt Lake City, Provo, and Nephi segments of the central WFZ. We then model the cumulative (coseismic + postseismic) Coulomb stress changes (ΔCFS_{cum}) due to several paleoseismological events on the WFZ and surrounding faults, and we include it in the probabilistic seismic hazard calculations. Finally, we compare the two probabilistic models, with and without ΔCFS, and discuss the impact of the chosen physical and statistical parameters on our results. We show that regardless of any uncertainties in this approach, ΔCFS_{cum} strongly affects the time-dependent probability of a large earthquake on the Brigham City, Salt Lake City and Provo segments.

2. Late Holocene history of the central WFZ and surrounding faults

The WFZ is located at the boundary between the extensional Basin and Range province to the west and the more stable Colorado Plateau to the east (Figure 1). It extends north - south for ~ 350 km, from southern Idaho to central Utah, and it accommodates ~ 50% of the deformation across the eastern Basin and Range (*Chang et al.*, 2006). Based on geomorphic, structural, and paleoseismological studies, the WFZ has been divided into ten segments (*Machette et al.*, 1992; *McCalpin & Nishenko,* 1996), six of which (Brigham City, Weber, Salt Lake City, Provo, Nephi, Levan) define the central WFZ (Figure 1). These segments show evidence of late Holocene activity and are considered capable of $M \geq 7$ single-segment ruptures. Studies on several active faults near the WFZ have been conducted as well, and have identified events on the East Great Salt Lake fault and on the West Valley fault zone (*Dinter & Pechmann*, 2005; *DuRoss & Hylland*, 2015). In the following sections we introduce the available geologic and paleoseismological data for the central WFZ, the Great Salt Lake fault, and the West Valley fault zone. We describe in more detail the faults used as sources or receivers for Coulomb stress calculations, and for which faults we carried out probability calculations.

2.1 Paleoseismological data

2.1.1 Central WFZ: Brigham City segment

Based on reinterpretation of previous studies and data from new trench sites, *Personius et al.* [2012] found evidence for at least four surface-rupturing events in the last ~6000 years on the Brigham City segment (Table 1). The most recent earthquake is dated 2400 ± 300 years B.P., which represents the oldest documented most recent event for the six segments of the WFZ (Table 1). A younger event (~1100 years B.P.) has been identified by *DuRoss et al.* (2012) on the southern part of the segment and interpreted by these authors as evidence of a spillover rupture from the adjacent Weber segment.

2.1.2 Central WFZ: Weber segment

The Weber segment is characterized by a mostly linear fault trace (Figure 1). In order to define a chronology of surface-rupturing earthquakes for the entire segment, data from four trench sites (*Swan et al.,* 1980, 1981; *McCalpin et al.*, 1994; *Nelson et al.*, 2006; *DuRoss et al.*, 2009) were re-evaluated by *DuRoss et al.* (2011). These authors concluded that five surface-rupturing earthquakes occurred on the Weber segment in the last ~6000 years (Table 1), with the most recent event dated 600 ± 100 years B.P. In addition, the penultimate earthquake (1100 ± 600 years B.P.) of the Weber segment (*DuRoss et al.*, 2012) may have spilled over as a partial rupture on the southern part of the Brigham City segment.

2.1.3 Central WFZ: Salt Lake City segment

The Salt Lake City segment (Figure 1) is the most complex segment in the central WFZ. From north to south it is divided in three subsections, separated by left steps: the Warm Springs (WS), East Bench (EB), and Cottonwood (CW) sections (Figure 1) (*Personius & Scott*, 1992; *DuRoss & Hylland*, 2015). In a recent work, *DuRoss & Hylland* (2015) integrated data from previous paleoseismological investigations (*Swan et al.*, 1980; *Black et* *al.*, 1996; *McCalpin*, 2002) and concluded that at least seven surface-rupturing events occurred on the Salt Lake City segment in the last ~ 10000 years, the latest of which is dated 1300 ± 200 years B.P., and the four surface-rupturing events that occurred in the last 6,000 years are shown in Table 1. *McCalpin* (2002), based on a high-resolution stratigraphic record, interpreted a period of seismic quiescence on the Salt Lake City segment between about 17 and 9 ka. There is some uncertainty concerning the rupture lengths in these earthquakes, and concerning the overall behavior of this segment, because of the complexity of the structure and the less-than-ideal resolution of the data (*DuRoss & Hylland*, 2015).

2.1.4 Central WFZ: Provo segment

The Provo segment is the longest segment (~70 km) of the central WFZ and has a complex surface trace that includes at least three subsections (Machette et al., 1992; DuRoss et al., 2016) (Figure 1). Several paleoseismological studies have been carried out on this segment, including a ~12-m deep, ~105-m long "megatrench" located in the southern part (*Olig et al.*, 2011). Integrated data from different sites (*DuRoss et al.*, 2016) show evidence for at least five surface-rupturing earthquakes on this segment, with the most recent event at 600 ± 50 years B.P. (Table 1).

2.1.5 Central WFZ: Nephi segment

The Nephi segment is composed of two strands: a more complex northern strand, which is separated from the Provo segment by a ~8 km wide right step, and a more linear southern strand, which terminates near the town of Nephi (Figure 1). Paleoseismological data from several trench sites show evidence for at least six surface-rupturing events in the last ~6000 years (Table 1) (*Crone et al.*, 2014; *DuRoss et al.*, 2016, 2017). Due to the structural complexity of this segment, the possible interaction with the adjacent Provo segment is still unclear. Recent studies from *Bennett et al.* (2014; 2015) suggest a complex rupture for the most recent event on the Nephi segment (200 ± 70 years B.P.). This rupture scenario includes the southernmost strand of the Nephi segment, the southern part of the northern strand, and a spillover onto the southern part of the Provo segment.

2.1.6 Central WFZ: Levan segment

The central WFZ terminates with the ~43 km long Levan segment (Figure 1). Unlike the other segments of the WFZ, the Levan segment has very limited paleoseismological data. In fact, only two late Holocene events have been recognized (*Jackson* 1991), with the latest event dated at 1000 ± 100 years B.P. The limited data available precludes the inclusion of this segment in probability calculations.

2.1.7 West Valley fault zone

The antithetic West Valley fault zone consists mainly of two subparallel main faults (Figure 1). These faults, together with the Salt Lake City segment of the WFZ, form a graben in the northern part of the Salt Lake Valley (*DuRoss & Hylland*, 2015). Recent studies have shown evidence for at least three earthquakes in the last 6000 years, with the latest dated at 1400 ± 700 years B.P. (*Hylland et al.*, 2014; *DuRoss & Hylland*, 2014, 2015). These ages are similar to those of events on the Salt Lake City segment. Therefore, on the basis of this and of mechanical and geometric models, *DuRoss & Hylland* (2014, 2015) hypothesized synchronous ruptures of the West Valley fault zone and of the Salt Lake City segment.

2.1.8 Great Salt Lake fault

The Great Salt Lake fault is a west-dipping normal fault located beneath the central and southern part of the Great Salt Lake (Figure 1). Several seismic profiles crossing the fault show two main active segments: the Fremont segment in the north, and the Antelope segment in the south [*Dinter & Pechmann*, 2005]. Radiocarbon dating of hanging-wall sediments extracted from core constrain the latest surface-rupturing event on the Antelope segment to 586 ± 200 years B.P. (*Dinter & Pechmann*, 2005; *WGUEP*, 2016).

2.2 Slip rates

Knowledge of the tectonic loading acting on the faults is necessary for the implementation of ΔCFS in probabilistic seismic hazard calculations. In order to calculate tectonic loading, we need the slip rate of all faults involved.

Slip rates are derived from either geodetic or geologic data. *Friedrich et al.* (2003) carried out an extensive study on the WFZ aimed at comparing present-day deformation rates with cumulative vertical fault slip rates over multiple timescales. They observed a good agreement between geodetic rates (~20 years timescale) and Holocene geologic rates (10^3 years timescale). The same consistency has also been observed in geodetic studies that implement earthquake cycle effects (*Malservisi et al.*, 2003) and finite-strain models (*Chang et al.*, 2006). Finally, recent results from the WGUEP report (*WGUEP*, 2016) show an agreement between geodetic moment rates and geological/seismological moment rates predicted by the Wasatch Front seismic source model developed in the study. We use here geological displacement rates based on mean vertical displacements measured from the paleoseismological data available for the five main segments of the central WFZ (Table 1) (*DuRoss et al.*, 2016).

3 Methods

3.1 Probabilistic seismic hazard calculations

Time-dependent seismic hazard approaches are based on the assumption that because a fault is loaded to failure by plate motions, the probability of occurrence of an earthquake in a given time period depends on the time since the last event. Several probability distributions have been used, for example lognormal, Weibull, and Brownian passage time (BPT) (*Fitzenz & Nyst*, 2015). In the last ~10 years, the BPT model has been preferred (*Field et al.*, 2015) because a BPT distribution has a hazard rate that tends towards a constant at long elapsed times, and it is considered to better approximate the elastic rebound theory (*Matthews et al.*, 2002). The other models instead either monotonically increase (Weibull) or decrease asymptotically to zero (lognormal). Here, we use the BPT model to calculate the conditional probability of occurrence of an earthquake on each of the five main segments of the central WFZ in the next 50 years making the assumption that each segment produces a characteristic earthquake. The BPT probability is given by *Matthews et al.* (2002) as:

$$P(t \le T \le t + \Delta T) = \int_t^{t+\Delta T} \sqrt{\left(\frac{T_m}{2\pi CV^2 u^3}\right)}\, e^{\left(-\frac{(u-T_m)^2}{2CV^2 T_m u}\right)} du \qquad [1]$$

$$P(T_{elap} \le T \le T_{elap} + \Delta T | T > T_{elap}) = \frac{P(T_{elap} \le T \le T_{elap} + \Delta T)}{1 - P(0 \le T \le T_{elap})} \qquad [2]$$

where T_m is either the mean recurrence time, or the time between maximum expected earthquakes of similar size on the individual source faults. CV is the coefficient of variation, defined as the standard deviation of the recurrence time over the mean, T_{elap} is the time elapsed since the last event on the source fault, ΔT is the observation period (in our case 50 years), and T represents the actual position of the fault in the BPT curve.

In order to compare our results with a time-independent approach, we calculate for each fault segment the time-independent Poissonian probability of occurrence of a characteristic earthquake, which is given by:

$$P_{poiss} = 1 - e^{-t/Tm} \qquad [3]$$

where t is the observation period (50 years), and T_m is the mean recurrence time. Below we explain the approaches we adopted to define the average recurrence time (T_m), the coefficient of variation (CV), and the maximum magnitude (M_{max}) expected for each of the five main segments of the central WFZ.

3.1.1 Average recurrence time (T_m) and coefficient of variation (CV)

We used the paleoseismological data described in section 2.1 (Table 1) as input for the open source Matlab® *FiSH* tool *Recurrence Parameters* (*RP*) (*Pace et al.*, 2016) to calculate T_m and CV, given by the ratio $CV=\sigma/T_m$ (the standard deviation σ over the mean recurrence time) (*Visini & Pace*, 2014) for the Brigham City, Weber, Salt Lake City, Provo, and Nephi segments of the central WFZ. Considering the reconstructed seismic history of the fault segments, *RP* uses a Monte Carlo approach (e.g. *Parsons,* 2008), by performing *n* simulations of the earthquake catalogue (hereafter synthetic catalogues) with the age of each event randomly varying within their uncertainties. In total, 100000 synthetic catalogues were computed for each segment, and T_m and CV were extracted from each of them.

3.1.2 Maximum expected magnitude (M_{max})

Maximum expected earthquake magnitude is a required input in both time-dependent and time-independent earthquake probability calculations. Here we use the *FiSH* tool *Moment Budget* (MB) (*Pace et al.*, 2016) to define the characteristic maximum magnitude (M_{max}) and its standard deviation for each of the five segments of the central WFZ. The code uses different empirical and analytical relationships based on fault subsurface length, rupture area, seismic moment, and aspect ratio (*Wells & Coppersmith*, 1994), to calculate four values of M_{max} and standard deviation. The code then calculates the sum of the four different M_{max} values treated as probability density functions (SumD) and defines a mean M_{max} and a standard deviation that will be used in the probability calculations. The mean M_{max}, the time elapsed since the last event (T_{elap}), T_m, and CV are in turn used as input for the *FiSH* tool

Activity Rates (AR) (*Pace et al.*, 2016), the code that we used to calculate BPT and Poissonian earthquake probabilities.

3.2 Coulomb stress changes calculations

The concept of Coulomb stress change (ΔCFS) has been extensively applied in the past two decades to explore the spatial and temporal relationships among active faults (e.g., *King et al.*, 1994; *Stein et al.*, 1994, 1997; *Harris & Simpson*, 1998; *Stein*, 1999; *Parsons et al.*, 2000; *Marsan*, 2003; *Ma et al.*, 2005; *Toda et al.*, 2008).

The change in Coulomb failure stress (ΔCFS) due to an earthquake on a source fault is:

$$\Delta CFS = \Delta\tau - \mu' (\Delta\sigma_n) \qquad [4]$$

where $\Delta\tau$ is the change in shear stress (positive in the direction of receiver fault slip) for receiver faults calculated on the orientation and kinematics of either optimally oriented faults, or specified faults. μ' is the coefficient of effective friction, and $\Delta\sigma_n$ is the change in normal stress (positive when the receiver fault is unclamped). A positive ΔCFS encourages faulting and thus increases the likelihood of an earthquake, whereas a negative ΔCFS inhibits faulting and decrease the likelihood of an earthquake.

A combination of time-independent static (coseismic) and time-dependent quasi-static (postseismic) modeling is often used to explain earthquake interactions at different time-scales (*Freed*, 2005). Postseismic calculations take into account the redistribution of Coulomb stress due to viscoelastic relaxation of lower crust and upper mantle, which is thought to play an important role at time-scales longer than 5 years (e.g. *Chéry et al*., 2001; *Pollitz et al.,* 2003; *Lorenzo-Martín et al*., 2006; *Ali et al*., 2008; *Shan et al.,* 2013;

Verdecchia & Carena, 2015; *Bagge et al.*, 2018). In our case, we operate at an earthquake-cycle time-scale (~1000 years), and thus we consider both coseismic and postseismic stress changes. We calculate the cumulative (coseismic + postseismic) Coulomb stress changes (ΔCFS_{cum}) on each of the five segments of the central WFZ during the time between their most recent event and the present-day. Our approach is based on the simplification that following a large earthquake, the Coulomb stress on the segment responsible for the event drops to zero, and the subsequent events on neighboring faults may modify its state of stress. For instance, if we consider that the most recent event on the Brigham City segment was ~2400 years B.P., all events on surrounding segments that postdate 2400 years B.P. may have modified the state of stress on the Brigham City segment.

Once the maximum ΔCFS_{cum} for each segment has been calculated, it can be applied to the time-dependent earthquake probability calculations. This could be done in two ways, as explained by *Stein et al.* (1997) and *Toda et al.* (1998). The first option requires a modification of T_m:

$$\mathrm{T'}_{\mathrm{m}} = \mathrm{T}_{\mathrm{m}} - (\Delta\mathrm{CFS}/\dot{\tau}) \qquad [5]$$

Whereas the second option requires a modification of T_{elap}

$$T'_{elap} = T_{elap} + (\Delta\mathrm{CFS}/\dot{\tau}) \qquad [6]$$

where $\dot{\tau}$ is the tectonic loading.

We computed the tectonic loading by using the Late Holocene slip rate values discussed in section 2.2. We extended the fault plane to a depth of 150 km, into the upper mantle in order to avoid boundary effects, locked the fault between the surface and 15 km depth (zero slip), and applied the long-term slip rates values between 15 and 150 km depth. The stress is thus transferred to the locked part of the fault (*Stein et al.*, 1997; *Cowie et al.*, 2013), where maximum interseismic ΔCFS are located at the base of the seismogenic depth (15 km) and decrease toward shallower depths. Because of this heterogeneous distribution of interseismic ΔCFS on the fault plane, we used an average value calculated between 9 and 15 km depth for each segment. For these calculations we used the same fault geometry and kinematics of the coseismic and postseismic ΔCFS models, and therefore considered variable strikes. We calculated the tectonic loading for each of the five studied segments of the central WFZ with the software *Coulomb 3.3* (*Toda et al.*, 2011) and the coseismic and postseismic ΔCFS with *PSGRN/PSCMP* (*Wang et al.*, 2006). *PSGRN/PSCMP* (*Wang et al.*, 2006) is a multilayered viscoelastic half-space based code, and it requires a rheologic model of the lithosphere as an input. We used the rheologic model defined by *Chang et al.* (2013) for the Intermountain Seismic Belt. These authors, based on trilateration and GPS data from 1973 to 2000, inferred a Maxwell rheology with 16 km of elastic upper and middle crust. A 14 km-thick lower crust and a 70 km-thick upper mantle were modeled as viscous layers with viscosity values of 10^{21} Pa·s and 10^{19} Pa·s, respectively. A range of effective friction coefficients (μ') between 0.2 and 0.8 is usually considered in studies of earthquake interactions (e.g. *Shan et al.*, 2013; *Verdecchia & Carena*, 2015). Here, we use an average single value of μ' equal to 0.4 in both ΔCFS_{cum} and tectonic loading calculations.

3.3 Fault geometry and slip models for paleoseismological earthquakes

The ΔCFS distribution due to an earthquake depends on the geometry and slip distribution of source faults, and on the geometry and kinematics of receiver faults. When we model paleoseismological earthquakes, these parameters have significant uncertainties due to the quality and density of the available paleoseismological data. For each of the five segments of the central WFZ, vertical displacement data for each paleoseismological event exist at multiple locations (*DuRoss*, 2008; *DuRoss et al.*, 2016, and references therein), therefore, we used these to better constrain the slip distribution of the earthquakes in our models. For the Levan segment, the West Valley fault zone, and the Great Salt Lake fault, we used the measured single-event coseismic offsets (*Jackson*, 1991; *DuRoss & Hylland*, 2015; *Dinter & Pechmann*, 2005) to build a slip model, assuming a tapered distribution with maximum values at the center of the fault. For the WFZ, the dip angle and its possible changes with depth are uncertain, and several fault geometries based on different data types have been proposed in the past 20 years (see discussion in *WGUEP*, 2016). Paleseismological data (*McCalpin et al.*, 1994) and earthquake moment tensors (*Doser & Smith*, 1989) indicate a high-angle (~70°), planar geometry. On the other hand, seismic reflection data indicate a listric geometry (6°-30°) merging into an older low-angle fault, likely a reactivated thrust fault, at shallow depths (*Smith & Bruhn*, 1984; *Velasco et al.*, 2010). Based on thickness of the sedimentary fill in the Salt Lake Valley and the projected position of the preextension paleosurface, *Friedrich et al.* (2003) inferred an average dip of ~20° - 30° for the active trace at depth, in agreement with the seismic reflection data (*Smith & Bruhn*, 1984). We adopt a planar geometry and a 50° dip angle for the WFZ, in following the 50° ± 10° value proposed by the *Basin and Range Province Earthquake Working Group* (*Lund*, 2012), the 50° ± 15° value proposed in the WGUEP report (*WGUEP*, 2016), and consistent with analyses of large historical Basin and Range earthquakes. This choice is also justified by the fact that we finally compare our probability results with those calculated in the WGUEP report. We set the locking depth at 15 km, based on the maximum depth of seismicity in the area (*Arabasz et al.*, 1992; *WGUEP*, 2016).

4. Results

Starting with the Brigham City segment, we modeled the ΔCFS_{cum} on each of the five segments of the central WFZ, between their most recent event and present-day (Figure 2). Because of the importance of strike variations in ΔCFS modeling (*Mildon et al*., 2016), we calculated stress changes on the Provo segment using two different orientations, one related to its southern part, and one related to its northern part. Figure 2 shows ΔCFS resolved on an average strike, dip, and rake for each segment, and on the strike of the southern part of the Provo segment. Calculations on the northern part of Provo segment are shown in Figure S1. We then computed the time-dependent and time-independent probabilities of occurrence of a characteristic earthquake on these segments, and finally recalculated the time-dependent probability by adding the effect of ΔCFS_{cum}. Because the most recent earthquake on the Nephi segment is the youngest of all, this segment has not been affected by Coulomb stress changes, and therefore the time-dependent probability calculated for the Nephi segment is the only one to which ΔCFS_{cum} does not apply.

4.1 Cumulative ΔCFS in the central WFZ

The most recent event on the Brigham City segment is the oldest of all the most recent events identified on any of the central WFZ segments (2400 +/- 300 years B.P., Table 1). Figure 2a shows that the largest positive ΔCFS_{cum} (~11 bars) (Table 2) on the Brigham City segment is located in its southern part, while ~2 bars have accumulated on its northern part. This is due to the effect of the most recent and the penultimate events (both younger than ~1100 years B.P.) that occurred on the adjacent Weber segment. Earthquakes on the other source faults are too distant to have a large effect on the Brigham City segment.

Because of the uncertainties in dating events, we explored two different scenarios for the Weber segment: (1) the most recent events on the Provo and Great Salt Lake segments are older than the most recent event on the Weber segment, and (2) the latest rupture on the Weber segment is older than the Provo and Great Salt Lake most recent events (Figure 2b). In the first case only the most recent event on the Nephi segment is part of the model, with no effects on the Weber segment because of the large distance between the two segments. In the second case, however, the most recent event on the Great Salt Lake fault transfers negative ΔCFS_{cum} (-5.2 bar) (Table 2) to the Weber segment, whereas the Provo segment is not close enough to produce an effect on the Weber segment (Figure 2b).

The most recent events on the Weber and Provo segments, and on the Great Salt Lake fault, strongly affect the Salt Lake City segment. These earthquakes produce positive stress changes larger than 10 bars (Table 2) in the northern and southern parts of the Salt Lake City segment (Figure 2c). The largest stress change (~11 bars) is on the southernmost part of the Salt Lake City segment, where *DuRoss et al.* (2018) document evidence for two surface ruptures younger than the ~1300 years B.P. event on the central part of this segment.

Finally, the Nephi segment, which produced the youngest of all the paleoseismological earthquakes in the central WFZ, transferred significant positive ΔCFS_{cum} (12.5 bars) (Table 2) to the NE-SW-striking Provo segment, with maximum values in the region where the Provo segment bends nearly 90° from a NNW-SSE to a NNE-SSW direction (Figure 2d). Calculations resolved on a NW-SE orientation (northern Provo segment) are shown in Figure S1. Paleoevents on the Great Salt Lake fault and Weber segment did not produce any stress changes on the Provo segment.

4.2 50-Year probabilities for the central WFZ segments

Results from Monte Carlo simulations of paleoseismological data show similar values of recurrence time (T_m) for the five segments, ranging from 1068 years for the Nephi segment to 1468 years for the Provo segment (Figure 3, Table 1). Although all the segments have CV < 1, suggesting a quasi-periodic behavior, some small differences are noticeable among segments. Based on the results from the Monte Carlo simulations described in section 3.1.1, we determined a range of CV between 0.1 and 0.4 for the Brigham City and Weber segments, between 0.3 and 0.5 for the Salt Lake City segment, between 0.3 and 0.6 for the Provo segment, and between 0.2 and 0.5 for the Nephi segment (Figure 3, Table 1). The maximum magnitudes (M_{max}) calculated for each of the five segments range from a minimum of 7.0 ± 0.2 for the Brigham City, Salt Lake City and Nephi segments to a maximum of 7.2 ± 0.2 for the Provo segment (Figure S2, Table 1). Using T_m, CV, and M_{max} as input parameters we determined the time-dependent (BPT) probability of a characteristic earthquake (M_{max} ± SD) for each segment of the central Wasatch fault for the next 50 years.

Our results show that the highest time-dependent probability of occurrence is for the Brigham City and Salt Lake City segments. For the former, probability ranges between 12% (CV = 0.4) and 79% (CV = 0.1) (Figure 4a, Table 3), whereas for the latter, probability is between 6% (CV = 0.5) and 9% (CV = 0.3) (Figure 5a, Table 3). In both cases the time-independent probability is lower than the time-dependent one (Figures 4a and 5a, Table 3). The Provo segment has time-dependent probability that ranges between 0.8% (CV = 0.3) and 3.9% (CV = 0.6) (Figure 6a, Table 3), and the for the Weber segment we computed time-dependent probability between zero and 2.1% (Figure 7a, Table 3). For the Provo and Weber segments, the variations between time-dependent and time-independent probability are comparable. Both the Provo and the Weber segments have a Poissonian probability of 3.5%. Finally, we determined a time-dependent probability very close to zero for the Nephi segment, against the 4.2% computed with a Poissonian approach (Figure 8, Table 3).

4.3 The effect of ΔCFS_{cum}

As already mentioned in section 3.2 (Equations 5 and 6), the implementation of ΔCFS in probabilistic seismic hazard models requires the knowledge of the tectonic loading ($\dot{\tau}$) acting on the studied faults. We calculated values of tectonic loading for the central WFZ that range between 0.036 bar/year (Salt Lake City segment) and 0.051 bar/year (Provo segment) (Figure S3, Table 2).

The Brigham City segment has the highest time-dependent probability of producing a characteristic earthquake in the next 50 years. The choice of whether we include ΔCFS by changing the elapsed time (T_{elap}) rather than by changing the recurrence time (T_m) has a significant effect on the resulting probability. For the Brigham City segment, the probability change is very small when T_{elap} is modified, whereas it is 13% to 39% higher when the T_m is modified (Figure 4, Table 3). The Weber segment is the only one that has been affected by negative rather than positive ΔCFS_{cum}. Decreases in probability (from 2.1% to 1.1%) are however only substantial for CV = 0.4 (Figure 7, Table 3). Like for the Brigham City segment, the ΔCFS_{cum} impact on the earthquake probability for the Salt Lake City segment is heavily dependent on the approach used. By modifying T_{elap}, we calculated a 30% increase in the probability (from 9% to 11.5%) for CV equal to 0.3, but a 70% increase (from 9% to 15.4%) can be obtained by modifying T_m instead (Figure 5, Table 3).

According to our results, the largest effect of introducing ΔCFS_{cum} is for the Provo segment, where the probability increases by up to five times (Figure 6, Table 3). The largest probability values for this segment (5.9%) is the result of a model with CV = 0.6 and an approach based on modification of T_m (Figure 6, Table 3). We obtained similar results using a lognormal probability distribution (Table S1).

5. Discussion

5.1 Significance of observed stress patterns on the central Wasatch Fault Zone

Because of the geometry of the fault network (along-strike alignment of normal faults), and our modeling assumptions (single-segment ruptures), high values of positive ΔCFS_{cum} ($\geq$ 10 bar) have accumulated on the segment ends of the Brigham City and Salt Lake City segments (Figure 2a, c), in agreement with the results from *Bagge et al.* (2018). On the Provo segment, regardless of the receiver fault geometry, maximum positive stress changes are localized on the fault bend (Figure 2d and Figure S1) due to the effect of the most recent event on the Nephi segment, which partially ruptured the southern part of the Provo segment. Negative ΔCFS_{cum} instead is transferred between the Great Salt Lake fault and the Weber segment, because they are parallel to each other (Figure 2b). Antithetic structures like the West Valley fault zone may encourage faulting on the Weber segment, but this effect is negligible compared to that of the other faults nearby (Great Salt Lake fault and Salt Lake City segment).

An important parameter that can change our results is the temporal order of the recorded paleoevents. However, as already described in section 4.1, such uncertainties only affect the results on the Weber segment, for which we examined two different scenarios with a different order of occurrence of the earthquakes on the Great Salt Lake fault, Provo segment, and Weber segment. Both scenarios are equally possible and therefore we do not choose one over the other.

In cases like the WFZ, where faults or segment terminations are very close to one another, the estimated extent of the coseismic rupture could affect results. Because here we modeled paleoseismological events, the information about rupture termination is strongly dependent on the number of paleoseismic sites available along each fault segment. Rupture extents are relatively well-known for the Brigham City (*DuRoss et al.*, 2012; *Personius et al.*,

2012) and Weber (*DuRoss et al.*, 2011; 2012) segments. The southern extent of the penultimate event on the Weber segment (1100 ± 600 years B.P.), which is modeled here as potential stress source for the Brigham City segment (Figure 2), is unclear (*DuRoss et al.*, 2016). However, whether the southern part of the Weber segment is included in the rupture model of this event is not important, as it would not significantly change the amount of ΔCFS_{cum} accumulated on the adjacent Brigham City segment, which depends on the location of the northern tip of the Weber segment rupture. On the other hand, according to the uncertainties in dating the penultimate event on the Weber segment, *DuRoss et al.* (2011) suggested that its southern part may have produced a partial rupture of the Weber segment at ~900 years B.P. If this is the case, this event may have further increased the stress on the adjacent Salt Lake City segment.

The rupture behavior of the Salt Lake City segment is particularly complex. From north to south the Salt Lake City segment is divided in three subsections: the Warm Springs, East Bench, and Cottonwood sections (*Personius & Scott*, 1992; *DuRoss & Hylland*, 2015). Whereas the most recent event (1300 ± 200 years B.P.) has been identified on the southernmost section (Cottonwood) of the segment, there is no trace of this earthquake in a trench site located in the East Bench section, and no paleoseismic data exist for the northernmost Warm Springs section (*DuRoss & Hylland*, 2015). Two different scenarios have therefore been proposed by *DuRoss & Hylland* (2015). In the first, the most recent event ruptured both the Cottonwood and East Bench section, but in the East Bench the event could not be identified due to the position of the trench site, located at the northernmost extent of the rupture. In the second scenario, the Cottonwood rupture represents a spillover of a large event originated on the Provo segment. Although paleoearthquake age ranges strongly support the first scenario, there is no evidence for excluding the second scenario. Modeling ΔCFS_{cum} with the second scenario for the most recent event on the Salt Lake City segment would result in a high value of ΔCFS_{cum} on the East Bench and Warm Springs sections, and negative ΔCFS_{cum} on the Cottonwood section.

The most recent event on the Nephi segment has also produced a complex surface rupture, with a possible spill-over on the adjacent Provo segment (*Bennett et al.*, 2014; 2015) as we described in section 2.1.5. Some doubts, however, exist on the age of the event detected on the southernmost part of the northern strand of the Nephi segment (Santaquin site) (*DuRoss et al.*, 2008). In our model, this part of the Nephi segment ruptures as part of the Nephi most recent event (~200 years B. P.). Another possible scenario arises if the event at the Santaquin site is actually older and of age similar to that of the most recent event on the Provo segment (~600 years B. P.). In this second case, the southernmost part of the northern strand of the Nephi segment would represent a spill-over of the Provo segment earthquake. In either case, the amount of ΔCFS_{cum} accumulated on the Provo segment due to the Nephi most recent event would not change.

If single-segment ruptures are most common along the central WFZ, then the segment boundary zones could be important locations of rupture initiation (consistent with *King & Nabelek* (1985)). However, as in the case of the Provo segment, positive stress changes may accumulate on fault bends when complex ruptures occur (e.g., Nephi segment most recent event). Therefore, further testing of stress concentrations along the segments using more complex rupture scenarios is warranted.

5.2 Testing and exploring the recurrence time (T_m) and its coefficient of variation (CV)

The choice of the recurrence time (T_m) and its coefficient of variation (CV) can have a large influence on time-dependent probability calculations. In order to test the reliability of calculated T_m values we run an N-test (*Zechar et al.*, 2010), a sort of retrospective test which compares the annual earthquake rates observed from the paleoseismological data with the annual earthquake rates calculated by the model, considering a Poissonian distribution. In particular, the N-test evaluates if the sum of predicted earthquakes in all time-space-magnitude bins (N_{fore}) is consistent with the number of target earthquakes observed (N_{obs}) over the entire testing region. For our specific case we considered both the probability of observing at least N_{obs} events:

$$\delta_1 = 1 - P((N_{obs}-1)|N_{fore}), \qquad [7]$$

and at most N_{obs} events:

$$\delta_2 = P(N_{obs}|N_{fore}). \qquad [8]$$

If δ_1 is very small, the forecast rate is too low (underprediction); and, if δ_2 is very small, the forecast rate is too high (overprediction). To test if our model passed the N-test we calculated the p-value:

$$\text{p-value} = 2 \min (\delta_1, \delta_2), \qquad [9]$$

if the calculated p-value is larger than a critical value of p-value = 0.025 the N-test is considered passed (*Zechar et al.*, 2010). Here, considering the Poissonian probabilities showed in Table 3, and 24 paleoseismological events occurred in a time-span of 6770 years in the whole fault system, we calculated δ_1 equal to 0.44, δ_2 equal to 0.55, and a p-value of 0.88. The results of the N-test confirm that the calculated T_m and relative Poissonian probabilities are in agreement with the observed data. Unfortunately, an N-test on a time-dependent model is not feasible because the N-test considers a Poissonian overall forecast rate.

A critical parameter for the time-dependent probability is the coefficient of variation of the recurrence time, and so it is important to explore the impact of that on earthquake probabilities. Several studies acknowledge that the coefficient of variation for earthquake recurrence intervals is poorly constrained (e.g. *Ellsworth et al.*, 1999; *Visini & Pace*, 2014), and small differences in the value can lead to order of magnitude differences in earthquake probability forecast. Based on results of Monte Carlo simulations of the available paleoseismological data (Figure 3), we decided to consider a range of values of CV for each studied segment of the central WFZ (Table 1 and 3). The largest impact of CV is evident in the probability calculated for the Brigham City segment. In fact, we noticed differences in probability up to 70% between CV = 0.1 and CV= 0.4. This is due to the fact that CV = 0.1 (periodic sequence) predicts significantly larger probabilities compared to other values (0.2, 0.3, 0.4), when $T_{elap} >> T_m$ (Figure 4). As already shown in section 5.2 and Table 3, the effect of CV on our final results is substantial for all the five segments of the central WFZ. Therefore, we believe that all the values of CV considered in this work are equally possible and thus choosing a single CV value for the entire central WFZ or even for each individual segment might underestimate or overestimate the final probabilities.

In Table 3 we compare our results with the single-segment rupture time-dependent probabilities calculated by the WGUEP report (*WGUEP*, 2016). The differences between the two results are mostly due to the choice of CV. In fact, the probability values from *WGUEP* (2016) are calculated adopting a CV range of 0.5 ± 0.2 based on a global CV (*Ellsworth et al.* 1999), while we used a segment-specific CV calculated from the paleoseismological record of each segment of the central WFZ.

5.3 Applying ΔCFS to probabilistic seismic hazard analysis: sensitivity of results to different methods

In section 3.2 we described two different methods commonly used to integrate ΔCFS in time-dependent probability calculations. In the first, Coulomb stress changes affect the recurrence time (T_m), whereas in the second they affect the elapsed time since the last event (T_{elap}). Although *Stein et al.* (1997) concluded that the two methods yield similar results, this is not true in cases when T_{elap} is significantly smaller or larger than T_m (*Parsons*, 2005; *Console et al.*, 2008). In our study this is particularly evident in the Brigham City segment. Here T_{elap} is more than twice T_m (Table 1), leading to large differences in probabilities calculated using the two different methods (Table 3). However, we found this discrepancy also when T_m is similar to T_{elap}, for example in the case of the Salt Lake City segment. Here, the probabilities calculated by modifying T_m are substantially larger than the ones predicted by modifying T_{elap} (15.4% against 11.5% for CV = 0.3) (Table 3). Finally, we did not find any obvious differences for the Weber and Provo segment, for which T_{elap} is nearly half of T_m.

As already discussed by *Parsons* (2005) and *Console et al.* (2008), there is no justification for choosing one method over another. The results from both methods should be considered as part of the uncertainties intrinsic to the integration of ΔCFS and probabilistic seismic hazard calculations. Here, in order to define a single probability of occurrence with its uncertainties, we calculated for each segment both the average and the standard deviation between the probability values in which ΔCFS is implemented (Table 3). A more conservative option would be to consider only the highest probability, which in our specific case corresponds to a probability calculated including ΔCFS with modified T_m (Table 3).

5.4 Model limitations and future work

The oversimplification of a model due to the lack of geological and seismological data in some regions is exemplified by the coseismic slip distribution that had to be adopted in our physical models. Because we are dealing with paleoseismological events, we modeled an along-strike tapered slip distribution constrained using the data available from each trench site. This is of course different from the more realistic heterogeneous distribution, but it is still the most reasonable assumption in these cases, where no instrumental or historical data are available. In section 3.3 we explored two competing models for the dip angle of the central WFZ: high-angle planar and low-angle listric. A reasonable question for this analysis is the influence of fault geometry on the ΔCFS calculations. Both variable strike and dip of source and receiver faults may have an impact on the final ΔCFS calculations (*King et al.*, 1994; *Mildon et al.*, 2016). *Verdecchia & Carena* (2016) compared stress patterns produced by normal faults with different geometries (high angle planar surface vs. listric surface), and concluded that for normal faults, the maximum values of coseismic ΔCFS do not change significantly when a constant-dip model and a more complex model are compared. Therefore, for our purposes of calculating maximum ΔCFS, adopting a different value for the fault dip will not change the final results dramatically. Because the tectonic loading is proportional to the slip rates of each fault segment, the slip rate variability can also be a source of uncertainties when calculating tectonic loading and as a consequence when calculating time-dependent probability with the effect of ΔCFS.

Another simplification that may affect our results concerns the rheology of the lithosphere used in calculating postseismic ΔCFS. We have used a rheologic model that does not account for horizontal heterogeneities, whereas in this region a significant rheological contrast might in fact exist between the footwall and the hanging wall of the central WFZ assuming that the fault is not listric at depth. *Thompson and Parsons* (2017) have also showed that isostatic effects could generate stress changes in the early postseismic stage.

Future work with finite elements instead of dislocation models should be carried out in order to better define the impact of lateral heterogeneities and isostasy on postseismic ΔCFS.

The last important consideration comes from uncertainties in the rupture lengths of past earthquakes and the statistical model used to calculate the probability of large earthquakes. We calculate probabilities only for single-segment rupture, and we did not apply the time-dependent method for different rupture scenarios. As described by *DuRoss et al.* (2016), the central WFZ paleoseismic data are generally consistent with single-segment ruptures, but multi-segment ruptures, or those crossing the segment boundaries (e.g., the penultimate rupture of the Weber segment that likely continued north onto the southernmost Brigham City segment), cannot be ruled out, because of uncertainties in event timing. Variability in the amount of displacement of the paleoseismological events also suggests the possibility of different rupture scenarios (*Lund,* 2005; 2006; *DuRoss,* 2008, *DuRoss et al.*, 2016). This has been confirmed by recent paleoseismological investigations (*Crone et al.*, 2014; *DuRoss et al.*, 2012; 2014; *Bennett et al.*, 2014; 2015), which have documented complex coseismic ruptures for the most recent events on the Weber and Nephi segments. Thus, although our modeling demonstrates important stress changes using the most common modes of central WFZ rupture, more detailed models based on alternative (e.g., more complex) rupture scenarios should be explored to better characterize the seismic hazard along the WFZ.

6. Conclusions

Using the results of Holocene earthquake timing and displacement data, we modeled the present-day coseismic and postseismic ΔCFS on the five main segments of the central WFZ accumulated in the period between the occurrence of their most recent event and the present-day. We also calculated ranges of CV and the probability of large earthquakes on these segments for the next 50 years, and then added ΔCFS in the same probability calculation, to verify whether it produces any significant changes.

Our results show that, regardless of whether or not we include ΔCFS in the probability calculations, the highest probabilities of occurrence in the central WFZ are predicted for the Brigham City and Salt Lake City segments. In addition, ΔCFS_{cum} models show that the Brigham City, the Salt Lake City, and the Provo segments have accumulated respectively 11.3, 10.8, and 12.5 bar of cumulative ΔCFS. These stress changes are concentrated at segments' ends (Brigham City and Salt Lake City segments), or at fault bends (Provo segment), suggesting that these zones could be possible locations of rupture initiation.

Finally, by integrating the cumulative ΔCFS and probabilistic seismic hazard analysis, we observed a substantial increase in probability for the Brigham City, Salt Lake City, and Provo segments when the effect of paleoseismological events is implemented in the probability calculations. These results indicate that the seismic hazard connected with single-segment ruptures on the central WFZ might be underestimated, if the effects of stress changes are not considered.

Acknowledgments

We thank Anke Friedrich, Jaime Delano, Keith Lucey, the Editor Eiichi Fukuyama, and two anonymous reviewers for their comments which helped to improve the manuscript. Any use of a trade, firm, or product names is for descriptive purposes only and does not imply endorsement by the U.S. Government.

References

Ali, S. T., Freed, A. M., Calais, E., Manaker, D. M. & McCann, W. R., 2008. Coulomb stress evolution in Northeastern Caribbean over the past 250 years due to coseismic, postseismic and interseismic deformation: *Geophys. J. Int.*, 174, 3, 904-918.

Arabasz, W. J., Pechmann, J. C. & Brown, E. D., 1992. Observational seismology and the evaluation of earthquake hazards and risk in the Wasatch Front area, Utah, in *Assessment of Regional Earthquake Hazards and Risk along the Wasatch Front, Utah,* Geol. Surv. Prof. Pap. 1500, P. L. Gori and W. W. Hays (Editors), D1-D36.

Bagge, M., Hampel, A. & Gold, R. D., 2018. Modeling the Holocene slip history of the Wasatch fault (Utah): Coseismic and postseismic Coulomb stress changes and implications for paleoseismicity and seismic hazard, *GSA Bull.,* 131, 1, p. 43-57, doi:10.1130/B31906.1.

Bennett, S. E. K., Gold, R. D. & DuRoss, C. B., 2015. Evidence for non-persistent rupture terminations at central Wasatch Fault Zone segment boundaries, Utah, SSA Annual Meeting 2015, 86:2B, 671.

Bennett, S. E. K., DuRoss, C. B., Reitman, N. G., DeVore, J. R., Hiscock, A. I., Gold, R. D., Briggs, R. W. & Personius, S. F., 2014. Using paleoseismic trenching and LiDAR analysis to evaluate rupture propagation through segment boundaries of the central Wasatch Fault Zone, Utah, AGU Fall Meeting 2014, abstract T32B-08.

Black, B. D., Lund, W. R., Schwartz, D. P., Gill, H. E. & Mayes, B. H., 1996. Paleoseismic investigation on the Salt Lake City segment of the Wasatch fault zone at the South Fork Dry Creek and Dry Gulch sites, Salt Lake County, Utah, Special Studies, 92, 22 pp., Utah Geological Survey, Salt Lake City.

Black, B. D., Hecker, S., Hylland, M. D., Christenson, G. E., & McDonald, G. N., 2003. Quaternary fault and fold database and map of Utah, *Utah Geological Survey Map* 193DM, scale 1:500,000, CD-ROM.

Chang, W. L. & Smith, R. B., 2002. Integrated seismic-hazard analysis of the Wasatch Front, Utah, *Bull. Seism. Soc. Am.*, 92, 5, 1904-1922.

Chang, W. L., Smith, R. B. & Puskas, C. M., 2013. Effects of lithospheric viscoelastic relaxation on the contemporary deformation following the 1959 M_w 7.3 Hebgen Lake, Montana, earthquake and other areas of the intermountain seismic belt, *Geochem. Geophy. Geosy.*, 14, 1, 1-17, doi:10.1029/2012GC004424.

Chang, W. L., Smith, R. B., Meertens, C. M. & Harris, R. A., 2006. Contemporary deformation of the Wasatch fault, Utah, from GPS measurements with implications for interseismic fault behavior and earthquake hazard: observations and kinematic analysis, *J. Geophys. Res.*, 111, B11405, doi:10.1029/2006JB004326.

Chéry, J., Carretier, S.& Ritz, J.-F., 2001. Postseismic stress transfer explains time clustering of large earthquakes in Mongolia, *Earth Planet. Sci. Lett*., 194, 1, 277-286.

Console, R., Murru, M, Falcone, G. & Catalli, F., 2008. Stress interaction effect on the occurrence probability of characteristic earthquakes in Central Appennines, *J. Geophys. Res.*, 113, B08313, doi:10.1029/2007JB005418.

Cowie, P. A., Scholz, C. H., Roberts, G. P., Faure Walker, J. P. & Steer, P., 2013. Viscous roots of active seismogenic faults revealed by geologic slip rate variations, *Nat. Geosci.*, 6, 1036-1040, doi:10.1038/NGEO1991.

Crone, A. J., Personius, S. F., DuRoss, C. B., Machette, M. N. & Mahan, S. A., 2014. History of Late Holocene earthquakes at the Willow Creek site on the Nephi segment, Wasatch fault zone, Utah, in *Paleoseismology of Utah*, W. R. Lund (Editor), Vol. 25, *Utah Geol. Surv. Spec. Stud.* 151, 55 pp.

Dinter D. & Pechmann, J., 2005. Segmentation and Holocene displacement history of the Great Salt Lake fault, Utah, in *Proceedings Volume, Basin and Range Province*

Seismic Hazard Summit II, W. R. Lund (Editor), *Utah Geol. Survey Misc. Publ.*, 05-2, CD, 5 pp.

Doser, D.I. & Smith, R. B., 1989. An assessment of source parameters of earthquakes in the cordillera of the western United States, *Bull. Seismol. Soc. Am.*, 79, 1383–1409.

DuRoss, C. B., 2008. Holocene vertical displacement on the central segments of the Wasatch fault zone, Utah, *Bull. Seismol. Soc. Am.*, 98, 6, 2918–2933.

DuRoss C. B. & Hylland, M. D., 2015. Synchronous ruptures along a major graben-forming fault system: Wasatch and West Valley fault zones, Utah, *Bull. Seismol. Soc. Am.*, 105, 14-37, doi:10.1785/0120140064.

DuRoss C. B. & Hylland, M. D., 2014. Evaluating surface faulting chronologies of graben-bounding faults in Salt Lake Valley, Utah: New paleoseismic data from the Salt Lake City segment of the Wasatch fault zone and the West Valley fault zone, in *Paleoseismology of Utah*, C. B. DuRoss and M. D. Hylland (Editors), Vol. 24, *Utah Geol. Surv. Spec. Stud.* 149, 71 pp.

DuRoss, C. B., Bennett, S. E. K., Briggs, R. W., Personius, S. F., Gold, R. D., Reitman, N. G., Hiscock, A. I. & Mahan, S. A., 2018. Combining conflicting Bayesian models to develop paleoseismic records: an example from the Wasatch Fault Zone, Utah, *Bull. Seism. Soc. Am.*, 108, 6, 3180-3201, doi:10.1785/0120170302.

DuRoss C. B., Hylland, M. D., Hiscock, A., Personius, S. P., Briggs, R., Gold, R. D, Beukelman, G., McDonald, G. N., Erickson, B., McKean, A., Angster. S., King, R., Crone, A. J. & Mahan, S., 2017. Holocene surface-faulting earthquakes at the SpringLake and North Creek sites on the Wasatch Fault Zone: evidence for complex rupture of the Nephi segment, in *Paleoseismology of Utah*, Vol. 28, pp 1-119.

DuRoss C. B., Personius, S. P., Crone, A. J., Olig, S. S., Hylland, M. D., Lund, W. R. & Schwartz, D. P., 2016. Fault segmentation: new concepts from the Wasatch Fault Zone, Utah, USA, *J. Geophys. Res.*, doi: 10.1002/2015JB012519.

DuRoss, C. B., Hylland, M. D., Hiscock, A., Beukelman, G., McDonald, G. N., Erickson, B., McKean, A., Personius, S. F., Briggs, R., Gold, R. D., Angster, S., King, R., Crone, A. J. & Mahan, S. A., 2014. Paleoseismic investigation to determine the Mid-Holocene chronology of surface-faulting earthquakes on the Nephi segment of the Wasatch Fault Zone, Utah and Juan counties, Utah, *U.S. Geological Survey, NEHRP final technical report,* award G12AP20076.

DuRoss, C. B., Personius, S. F., Crone, A. J., McDonald, G. N. & Briggs, R. W., 2012. Late Holocene earthquake history of the Brigham City segment of the Wasatch fault zone at the Hansen Canyon, Kotter Canyon, and Pearson Canyon trench sites, Box Elder County, Utah, in *Paleoseismology of Utah,* Utah Geol. Surv. Spec. Stud. 142, W. R. Lund (Editor), Vol. 22, 62.

DuRoss, C. B., Personius, S. F., Crone, A. J., Olig, S. S. & Lund, W. R., 2011. Integration of paleoseismic data from multiple sites to develop an objective earthquake chronology: Application to the Weber segment of the Wasatch fault zone, Utah, *Bull. Seismol. Soc. Am.*, 101, 6, 2765-2781.

DuRoss, C. B., Personius, S. F., Crone, A. J., McDonald, G. N. & Lidke, D. J., 2009. Paleoseismic investigation of the northern Weber segment of the Wasatch fault zone at the Rice Creek trench site, North Ogden, Utah, in *Paleoseismology of Utah*, W. R. Lund (Editor), Vol. 18, *Utah Geol. Surv. Spec. Stud.*, 130, 37 pp.

DuRoss, C. B., McDonald, G. N. & Lund, W. R., 2008. Paleoseismic investigation of the northern strand of the Nephi segment of the Wasatch fault zone at Santaquin, Utah, in

Paleoseismology of Utah, W. R. Lund (Editor), Vol. 17, *Utah Geol. Surv. Spec. Stud.*, 124, 33pp.

Ellsworth, W. L., Matthews, M. V., Nadeau, R. M., Nishenko, S. P., Reasenberg, P. A. & Simpson, R. W., 1999. A physically based earthquake recurrence model for estimation of long-term earthquake probabilities, *U.S. Geological Survey Open-FIle Report*, 99-522.

Field, E. H., Biasi, G. P., Bird, P., Dawson, T. E., Felzer, K. R., Jackson, D. D., Johnson, K. M., Jordan, T. H., Madden, C., Michael, A. J., Milner, K. R., Page, M. T., Parsons, T., Powers, P. M., Shaw, B. E., Thatcher, W. R., Weldon II, R. J. & Zeng, Y., 2015. Long-term time-dependent probabilities for the third Uniform California Earthquake Rupture Forecast (UCERF3), *Bull. Seismol. Soc. Am.*, 105, 2A, doi:10.1785/0120140093.

Fitzenz D. D. & Nyst, M., 2015. Building time-dependent earthquake recurrence models for probabilistic risk computations, *Bull. Seismol. Soc. Am.*, 105, 1, 120-133, doi:10.1785/0120140055.

Freed, A. M., 2005. Earthquake triggering by static, dynamic and postseismic stress transfer, *Annu. Rev. Earth Planet. Sci.*, 33, 335-367.

Friedrich, A. M., Wernicke, B. P., Niemi, N. A., Bennett, R. A. & Davis, J. L., 2003. Comparison of geodetic and geologic data from the Wasatch region, Utah, and implications for the spectral character of Earth deformation at periods of 10 to 10 million years, *J. Geophys. Res.*, 108, B4, 2199, doi:10.1029/2001JB000682.

Hammond, W. C., Kreemer, C. & Blewitt, G., 2009. Geodetic constraints on contemporary deformation in the northern Walker Lane: 3. Central Nevada seismic belt postseismic relaxation, *Geol. S. Am. S.,* 447, 33-54.

Harris, R. A. & Simpson, R. W., 1998. Suppression of large earthquakes by stress shadows: A comparison of Coulomb and rate-and-state failure, *J. Geophys. Res.*, 103, B10, 24439-24451.

Hylland, M. D., DuRoss, C. B., McDonald, G. N., Olig, S. S., Oviatt, C. G., Mahan, S. A., Crone, A. J. & Personius, S. F., 2014. Late Quaternary paleoseismology of the West Valley fault zone, Utah: Insights from the Baileys Lake trench site, in *Evaluating Surface Faulting Chronologies of Graben-Bounding Faults in Salt Lake Valley, Utah: New Paleoseismic Data from the Salt Lake City Segment of the Wasatch Fault Zone and the West Valley Fault Zone*, in Paleoseismology of Utah, C. B. DuRoss and M. D. Hylland (Editors), Vol. 24, Utah Geol. Surv. Spec. Stud. 149, 41–71.

Jackson, M., 1991. Number and timing of Holocene paleoseismic events on the Nephi and Levan segments, Wasatch fault zone, Utah, in *Paleoseismology of Utah*, W. R. Lund (Editor), Vol. 3, *Utah Geol. Surv. Spec. Stud.* 78, 23 pp.

King, G. C. & Nabelek, J., 1985. The role of bends in faults in the initiation and termination of earthquake rupture, *Science*, 228, 984-987.

King, G. C., Stein, R. S. & Lin, J., 1994. Static stress changes and the triggering of earthquakes:*Bull. Seism. Soc. Am.*, 84, 3, 935-953.

Lorenzo-Martín, F., Roth, F. & Wang, R., 2006. Elastic and inelastic triggering of earthquakes in the North Anatolian Fault zone, *Tectonophysics*, 424, 3, 271-289.

Lund, W. R., (Editor), 2012. Basin and Range Province Earthquake Working Group II – Recommendations to the U.S. Geological Survey National Seismic Hazard Mapping Program for the 2014 update of the National Seismic Hazard Maps: *Utah Geological Survey Open-File Report*, 591, 17 p.

Lund, W. R., 2005. Consensus preferred recurrence-interval and vertical slip-rate estimates: review of Utah paleoseismic-trenching data by the Utah Quaternary Fault Parameters Working Group, *Utah Geol. Surv. Bull.*, 130, 109.

Lund, W. R., (Editor), 2006. Basin and Range Province Earthquake Working Group seismic-hazard recommendations to the U.S. Geological Survey National Seismic Hazard Mapping Program, *Utah Geol. Surv. Open-File Rept.*, 477, 23 pp.

Ma, K. F., Chan, C. H. & Stein, R. S., 2005. Response of seismicity to Coulomb stress triggers and shadows of the 1999 Mw= 7.6 Chi-Chi, Taiwan, earthquake, *J. Geophys. Res.*, 110, B5.

Marsan, D., 2003. Triggering of seismicity at short timescales following Californian earthquakes, *J. Geophys. Res.*, 108, B5.

Machette, M. N., Personius, S. F. & Nelson, A. R., 1992. Paleoseismology of the Wasatch fault zone: A summary of recent investigations, interpretations, and conclusions, in *Assessment of Regional Earthquake Hazards and Risk along the Wasatch Front, Utah*, edited by P. L. Gori and W. W. Hays, *U.S. Geol. Surv. Prof. Pap.*, 1500-A-J, A1-A71.

Malservisi R., Dixon, T. H. & La Femina, P. C., 2003. Holocene slip rate of the Wasatch fault zone, Utah, from geodetic data: Earthquake cycle effects, *Geophys. Res. Lett.*, 30, 13, 1673, doi:10.1029/2003GL017408.

Matthews, M., Ellsworth, W. L. & Reasenberg, P. A., 2002. A Brownian model for recurrent earthquakes, *Bull. Seismol. Soc. Am.*, 92, 6, 2233-2250.

McCalpin, J. P., 2002. Post-Bonneville paleoearthquake chronology of the Salt Lake City segment, Wasatch fault zone, Utah, in *Paleoseismology of Utah*, Utah Geol. Surv. Misc. Pub. 02-9, vol. 11, edited by W. R. Lund, 46 pp., Utah Geological Survey, Salt Lake City, Utah.

McCalpin, J. P., Forman, S. L. & Lowe, M., 1994. Reevaluation of Holocene faulting at the Kaysville site, Weber segment of the Wasatch fault zone, Utah. *Tectonics* 13 (1), 1–16.

McCalpin, J. P. & Nishenko, S. P., 1996. Holocene paleoseismicity, temporal clustering, and probabilities of future large (M>7) earthquakes on the Wasatch fault zone, Utah, *J. Geophys. Res.*, 101, B3, 6233-6253.

Mildon, Z. K., Toda, S., Faure Walker, J. P. & Roberts, G. P., 2016. Evaluating models of Coulomb stress transfer: Is variable fault geometry important?, *Geophys. Res. Lett.*, 43, 12407-12414, doi:10.1002/2016GL071128.

Nelson, A. R., Lowe, M., Personius, S. F., Bradley, L. A., Forman, S. L., Klauk, R. & Garr, J., 2006. Holocene earthquake history of the northern Weber segment of the Wasatch fault zone, Utah, in *Paleoseismology of Utah*, Vol. 13, W. R. Lund (Editor), *Utah Geol. Surv. Misc. Pub.*, 05-8, 39 pp.

Olig, S. S., McDonald, G., Black, B. D., DuRoss, C. B., Lund, W. R., Hylland, M., Simon, D. B., Giraud, R. E. & Christenson, G. E., 2011. Extending the paleoseismic record of the Provo segment of the Wasatch fault zone, Utah, *U.S. Geological Survey, NEHRP final technical report,* award 02HQGR0109.

Pace, B., Visini F. & Peruzza, L., 2016. FiSH: MATLAB tools to turn fault data into seismic hazard models, *Seismol. Res. Lett.*, 87, 2A, 374-386, doi:10.1785/0220150189.

Pace, B., Bocchini, G. M. & Boncio, P., 2014. Do static stress changes of moderate-magnitude earthquake significantly modify the regional seismic hazard? Hints from the L'Aquila 2009 normal-faulting earthquake (Mw 6.3, central Italy), *Terra Nova*, 26, 6, 430-439, doi:10.1111/ter.12117.

Parsons, T., 2008. Monte Carlo method for determining earthquake recurrence parameters from short paleoseismic catalogs: example calculations for California, *J. Geophys. Res.*, 113, B03302, doi:10.1029/2007JB004998.

Parsons, T., 2005. Significance of stress transfer in time-dependent earthquake probability calculations, *J. Geophys. Res.*, 109, B05304, doi:10.1029/2003JB002667.

Parsons, T., Toda, S., Stein, R. S., Barka, A. & Dieterich, J. H., 2000. Heightened odds of large earthquakes near Istanbul: An interaction-based probability calculation, *Science*, 288, 5466, 661-665.

Personius S. F. & Scott, W. E., 1992. Surficial geologic map of the Salt Lake City segment and parts of adjacent segments of the Wasatch fault zone, Davis, Salt Lake, and Utah Counties, Utah, *U.S. Geol. Surv. Misc. Invest. Series Map I-2106*, scale 1:50000.

Personius, S. F., DuRoss, C. B. & Crone, A. J., 2012. Holocene behavior of the Brigham City segment: implications for forecasting the next large-magnitude earthquake on the Wasatch Fault Zone, Utah, *Bull. Seism. Soc. Am.*, 102, 6, 2265-2281, doi:10.1785/0120110214.

Pollitz, F., Vergnolle, M. & Calais, E., 2003. Fault interaction and stress triggering of twentieth century earthquakes in Mongolia, *J. Geophys. Res.*, 108, B10.

Shan, B., Xiong, X., Wang, R., Zheng, Y. & Yang, S., 2013. Coulomb stress evolution along Xianshuihe–Xiaojiang Fault System since 1713 and its interaction with Wenchuan earthquake, May 12, 2008, *Earth Planet. Sci. Lett.*, 377, 199-210.

Smith, R. B. & Bruhn, R. L., 1984. Intraplate extensional tectonics of the western U.S. Cordillera — inferences on structural style from seismic-reflection data, regional tectonics and thermal–mechanical models of brittle–ductile deformation. *J. Geophys. Res.*, 89 (B7), 5733–5762.

Stein, R. S., 1999. The role of stress transfer in earthquake occurrence, *Nature*, 402, 605-609.

Stein, R. S., Barka, A. & Dieterich, J., 1997. Progressive failure on the North Anatolian fault since 1939 by earthquake stress triggering, *Geophys. J. Int.*, 128, 594-604.

Stein, R. S., King, G. C. & Lin, J., 1994. Stress triggering of the 1994 M= 6.7 Northridge, California, earthquake by its predecessors, *Science*, 265, 5177, 1432-1435.

Swan, F. H., III, Schwartz, D. P. & Cluff, L. S., 1980. Recurrence of moderate to large magnitude earthquakes produced by surface faulting on the Wasatch fault zone, Utah, *Bull. Seismol. Soc. Am.*, 70, 1431–1462.

Swan, F. H., III, Schwartz, D. P., Hanson, K. L., Knuepfer, P. L. & Cluff, L. S., 1981. Study of earthquake recurrence intervals on the Wasatch fault at the Kaysville site, Utah, U.S. *Geol. Surv. Open-File Rep.*, 81-228, 30 pp.

Thompson, G. A. & Parsons, T, 2017. From coseismic offsets to fault-block mountains, *Proc. Nat. Acad. Sci. USA*, 114, p. 9820-9825, doi:10.1016/j.tecto.2012.01.026.

Toda, S., Stein, R. S., Sevilgen, V. & Lin J., 2011. Coulomb 3.3 graphic-rich deformation and stress-change software for earthquake, tectonic, and volcano research and teaching-user guide, *U.S. Geological Survey Open-File Report*, 2011-1060, 63 pp.

Toda, S., Lin, J., Meghraoui, M. & Stein, R. S., 2008. 12 May 2008 M= 7.9 Wenchuan, China, earthquake calculated to increase failure stress and seismicity rate on three major fault systems,*Geophys. Res. Lett.*, 35, 17.

Toda, S., Stein, R. S., Reasenberg, P., Dieterich, J. & Yoshida, A., 1998. Stress transferred by the 1995 Mw = 6.9 Kobe, Japan, shock: Effect on aftershocks and future earthquake probabilities, *J. Gephys. Res.*, 103(B10), 24543-24565.

Velasco M. S., Bennett, R. A., Johnson, R. A. & Hreinsdottir, S., 2010. Subsurface fault geometries and crustal extension in the eastern Basin and Range province, western U.S., *Tectonophysics*, 488, 131-142.

Verdecchia A. & Carena, S., 2016. Coulomb stress evolution in a diffuse plate boundary: 1400 years of earthquakes in eastern California and western Nevada, USA, *Tectonics*, 35, 1793-1811, doi:10.1002/2015TC004091.

Verdecchia, A. & Carena, S., 2015. One hundred and fifty years of Coulomb stress history along the California-Nevada border, USA, *Tectonics*, 34, 2, 213-231.

Visini, F. & Pace, B., 2014. Insights on a key parameter of earthquake forecasting, the coefficient of variation of the recurrence time, using a simple earthquake simulator, *Seism. Res. Lett.*, 85, 3, 703-713.

Wang, R., Lorenzo-Martín, F. & Roth, F., 2006. PSGRN/PSCMP—a new code for calculating co-and post-seismic deformation, geoid and gravity changes based on the viscoelastic-gravitational dislocation theory, *Computers & Geosciences*, 32, 4, 527-541.

Wells, D. L. & Coppersmith, K. J., 1994. New empirical relationships among magnitude, rupture length, rupture width, rupture area, and surface displacement, *Bull. Seism. Soc. Am.*, 84, 4, 974-1002.

Working Group on Utah Earthquake Probabilities (WGUEP), 2016. Earthquake probabilities for the Wasatch Front region in Utah, Idaho, and Wyoming, *Utah Geological Survey Miscellaneous Publication* 16-3, 164 p., 5 appendices.

Zechar, J. D., Gerstenberger, M. C. & Rhoades, D. A., 2010. Likelihood-based tests for evaluating space-rate-magnitude earthquake forecasts, *Bull. Seism. Soc. Am.*, 100, 3, p. 1184-1195, doi: 10.1785/0120090192.

Figure captions

Figure 1. Map of Quaternary active faults in north-central Utah (*Black et al*., 2003). Thick black lines are the segments of the central Wasatch Fault Zone (WFZ). Red arrows indicate segment boundaries. Blue arrows indicate the boundaries of the three sections of the Salt Lake City segment. BC= Brigham City segment, WB=Weber segment, SLC=Salt Lake City segment, PR=Provo segment, NP=Nephi segment, LV=Levan segment, GSL=Great Salt Lake fault, WV=West Valley fault zone, WS=Warm Springs section, EB=East Bench section, CW=Cottonwood section, B&R=Basin and Range, CP=Colorado Plateau, UT=Utah, NV=Nevada, ID=Idaho. National Elevation Dataset available from the U.S. Geological Survey.

Figure 2. Cumulative (coseismic + postseismic) ΔCFS due to the earthquakes that have occurred since the most recent event of the receiver fault. Cumulative ΔCFS are calculated on the kinematics of (a) the Brigham City segment (BC), (b) the Weber segment (WB), (c) the Salt Lake City segment (SLC), (d) the southern part of the Provo segment (PR). Thick white lines are source faults; thick yellow lines are receiver faults; dashed black lines represent the depth-contour of the receiver fault at calculation depth where maximum ΔCFS are calculated. Refer to Table 2 for source earthquakes and receiver faults. NP=Nephi segment, LV=Levan segment, GSL=Great Salt Lake fault, WV=West Valley fault zone. National Elevation Dataset available from the U.S. Geological Survey.

Figure 3. Paleoseismological data and results from the Monte Carlo simulations for (a, b) the Brigham City segment, (c, d) the Weber segment, (e, f) the Salt Lake City segment, (g, h) the Provo segment, and (i, j) the Nephi segment. T_m and CV are respectively the mean recurrence and the coefficient of variation. Hit count represents the number of Monte Carlo simulations.

Figure 4. BPT probability curves calculated for the Brigham City segment for the next 50 years using different values of coefficient of variation (CV). Red circles represent the BPT

probabilities when ΔCFS is not considered. Blue circles represent BPT probabilities when ΔCFS is considered using (a) the approach based on modified T_{elap}, and (b) the approach based on modified Tm. Dashed black line is the time-independent Poisson probability. T_{elap} and T_m are respectively the time elapsed since the most recent event, and the mean recurrence time.

Figure 5. BPT probability curves calculated for the Salt Lake City segment for the next 50 years using different values of coefficient of variation (CV). Red circles represent the BPT probabilities when ΔCFS is not considered. Blue circles represent BPT probabilities when ΔCFS is considered using (a) the approach based on modified T_{elap}, and (b) the approach based on modified T_m. Dashed black line is the time-independent Poisson probability. T_{elap} and Tm are respectively the time elapsed since the most recent event, and the mean recurrence time.

Figure 6. BPT probability curves calculated for the Provo segment for the next 50 years using different values of coefficient of variation (CV). Red circles represent the BPT probabilities when ΔCFS is not considered. Blue circles represent BPT probabilities when ΔCFS is considered using (a) the approach based on modified T_{elap}, and (b) the approach based on modified T_m. Dashed black line is the time-independent Poisson probability. T_{elap} and T_m are respectively the time elapsed since the most recent event, and the mean recurrence time.

Figure 7. BPT probability curves calculated for the Weber segment for the next 50 years using different values of coefficient of variation (CV). Red circles represent the BPT probabilities when ΔCFS is not considered. Blue circles represent BPT probabilities when ΔCFS is considered using (a) the approach based on modified T_{elap}, and (b) the approach based on modified T_m. Dashed black line is the time-independent Poisson probability. T_{elap}

and T_m are respectively the time elapsed since the most recent event, and the mean recurrence time.

Figure 8. BPT probability curves calculated for the Nephi segment for the next 50 years using different values of coefficient of variation (CV). Red circles represent the BPT probabilities. Dashed black line is the time-independent Poisson probability. T_{elap} and T_m are respectively the time elapsed since the most recent event, and the mean recurrence time.

Table 1. Input parameters used for probability calculations in the central WFZ

Segment	Paleoevents[a] (years B.P.)	T_m (years B.P.)	CV	T_{elap} (years)	Slip Rate[b] (mm/yr)	Length (km)	M_{max} ($\pm 1\sigma$)
Brigham City	B1: 2400 ± 300 B2: 3500 ± 200 B3: 4500 ± 500 B4: 5600 ± 600	1127	0.1 - 0.4	2465	1.6	41	7.0 ± 0.2
Weber	W1: 600 ± 100 W2: 1100 ± 600 W3: 3100 ± 300 W4: 4500 ± 300 W5: 5900 ± 500	1367	0.1 - 0.4	665	1.8	58	7.1 ± 0.2
Salt Lake City	S1: 1300 ± 200 S2: 2200 ± 200 S3: 4100 ± 200 S4: 5300 ± 200	1333	0.3 - 0.5	1365	1.3	45	7.0 ± 0.2
Provo	P1: 600 ± 50 P2: 1500 ± 400 P3: 2200 ± 400 P4: 4700 ± 300 P5: 5900 ± 1000	1468	0.3 - 0.6	665	2.0	70	7.2 ± 0.2
Nephi	N1: 200 ± 70 N2: 1200 ± 80 N3: 2400 ± 100 N4: 4000 ± 90 N5: 4700 ± 500 N6: 5700 ± 800	1068	0.2 - 0.5	265	1.8	44	7.0 ± 0.2

[a]Per-segment earthquake timing, based on integration of site earthquake data younger than 7 ka (*DuRoss et al.*, 2016). [b]Mean vertical slip rate, based on mean vertical displacement per segment divided by mean recurrence time (*DuRoss et al.*, 2016). T_m is the recurrence time, CV is the coefficient of variation, T_{elap} is the elapsed time since the last earthquake, M_{max} is the maximum expected magnitude.

Table 2. Calculated ΔCFS and its integration in time-dependent parameters.

Segment	Source Earthquakes[a]	Receiver[b] (deg)	ΔCFS_{cos}[c] (bar)	ΔCFS_{cum}[d] (bar)	$\dot{\tau}$ (bar/year)	$T_{elap}+\Delta CFS_{cum}$ (years)	$T_m+\Delta CFS_{cum}$ (years)
Brigham City	W1, W2, S1, P1, N1, LV, WV, GSL	161/50/-90	5.7	11.3	0.045	2716	876
Weber	S1, P1, N1, GSL	154/50/-90	-7.1	-5.2	0.049	559	1373
Salt Lake City	W1, W2, P1, N1, LV, GSL	168/50/-90	4.7	10.8	0.036	1665	1036
Provo	W1, N1, GSL	218/50/-90	10.5	12.5	0.051	910	1023
Nephi	/	/	0.0	0.0	0.048	265	1068

[a]Details in Table 1. [b]Strike/Dip/Rake. [c]Maximum coseismic ΔCFS located anywhere on the fault plane. [d]Maximum cumulative (coseismic + postseismic) ΔCFS located anywhere on the fault plane. $\dot{\tau}$ is the stressing rate. T_{elap} is the elapsed time since the last earthquake, T_m is the mean recurrence time.

Table 3. Probability of a single-segment rupture for the next 50 years (P_{50}), calculated on each of the five main segment of the central WFZ.

Segment	CV	P_{50}Poisson	P_{50}BPT	P_{50}BPT+ΔCFS$_{cum}$ (T'_{elap})	P_{50}BPT+ΔCFS$_{cum}$ (T'_m)	P_{50}BPT+ΔCFS$_{cum}$[a] (Avg ± SD)	P_{50}BPT WGUEP [2016][b]
Brigham City	0.1	3.9%	78.8%	80.0%	89.0%	39.9% ± 29.5%	7.5%
	0.2		34.1%	35.2%	44.3%		
	0.3		18.5%	18.9%	24.2%		
	0.4		12.0%	12.1%	15.5%		
Weber	0.1	3.5%	0.0%	0.0%	0.0%	0.4% ± 0.6%	2.0%
	0.2		0.0%	0.0%	0.0%		
	0.3		0.8%	0.2%	0.4%		
	0.4		2.1%	1.1%	1.4%		
Salt Lake City	0.3	3.3%	8.9%	11.5%	15.4%	10.4% ± 3%	6.1%
	0.4		7.3%	8.5%	11.2%		
	0.5		6.3%	6.8%	8.8%		
Provo	0.3	3.5%	0.8%	3.8%	3.3%	4.8% ± 0.9%	2.8%
	0.4		2.1%	4.8%	4.8%		
	0.5		3.2%	5.1%	5.6%		
	0.6		3.9%	5.1%	5.9%		
Nephi	0.2	4.2%	0.0%	0.0%	0.0%	0.1% ± 0.1%	0.5%
	0.3		0.0%	0.0%	0.0%		
	0.4		0.0%	0.0%	0.0%		
	0.5		0.3%	0.3%	0.3%		

[a]Average and standard deviation calculated between the probabilities in which stress changes are implemented. [b]Weighted average among results using CV = 0.3, 0.5, 0.7, and five different recurrence time (T_m) for each coefficient of variation (CV).

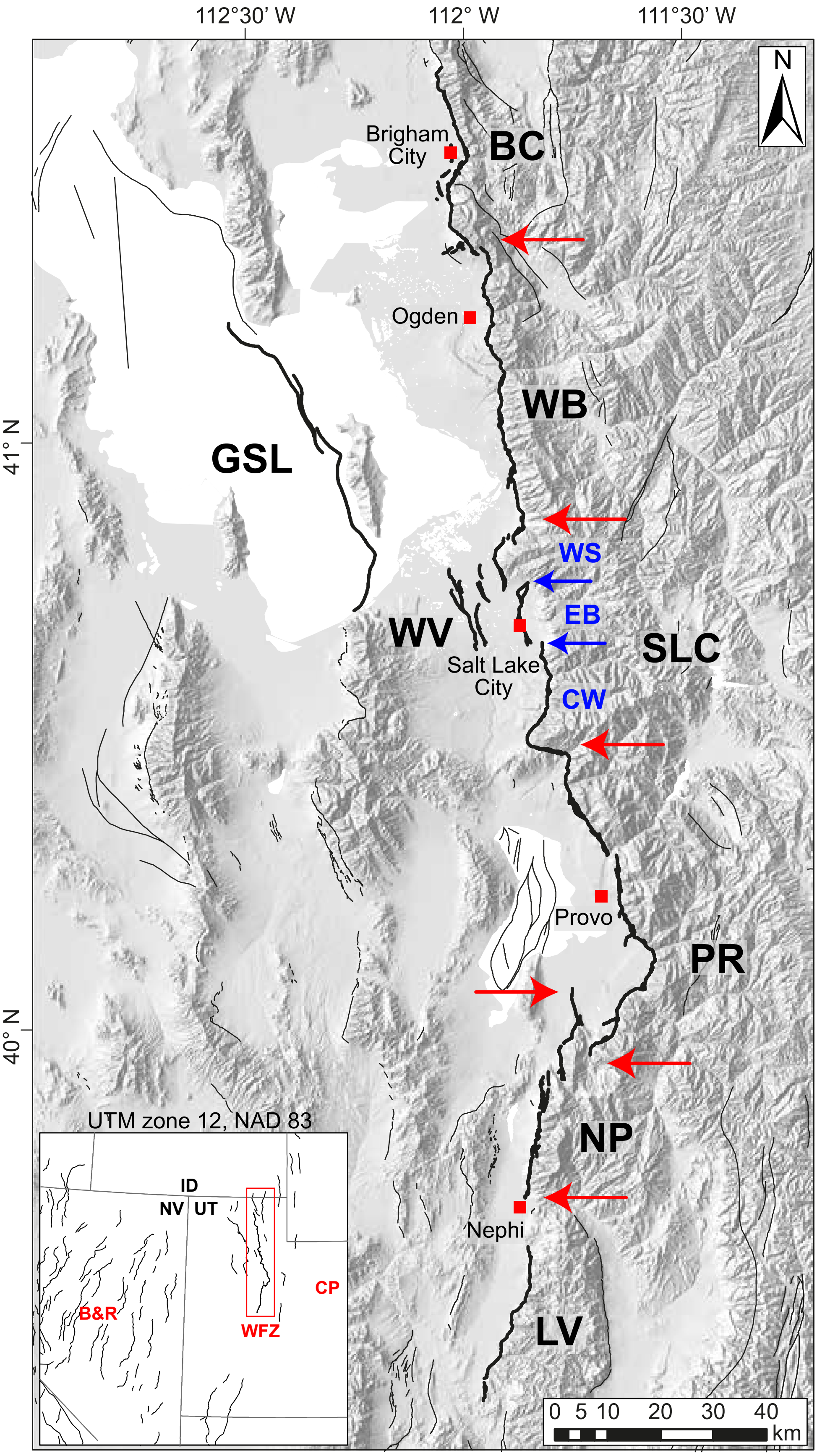

Figure 1. Map of Quaternary active faults in north-central Utah [*Black et al.*, 2003]. Thick black lines are the segments of the central WFZ. Red arrows indicate segment boundaries. Blue arrows indicate the boundaries of the three sections of the Salt Lake City segment. BC= Brigham City segment, WB=Weber segment, SLC=Salt Lake City segment, PR=Provo segment, NP=Nephi segment, LV=Levan segment, GSL=Great Salt Lake fault, WV=West Valley fault zone, WS=Warm Springs section, EB=East Bench section, CW=Cottonwood section, B&R=Basin and Range, CP=Colorado Plateau, UT=Utah, NV=Nevada, ID=Idaho. National Elevation Dataset available from the U.S. Geological Survey.

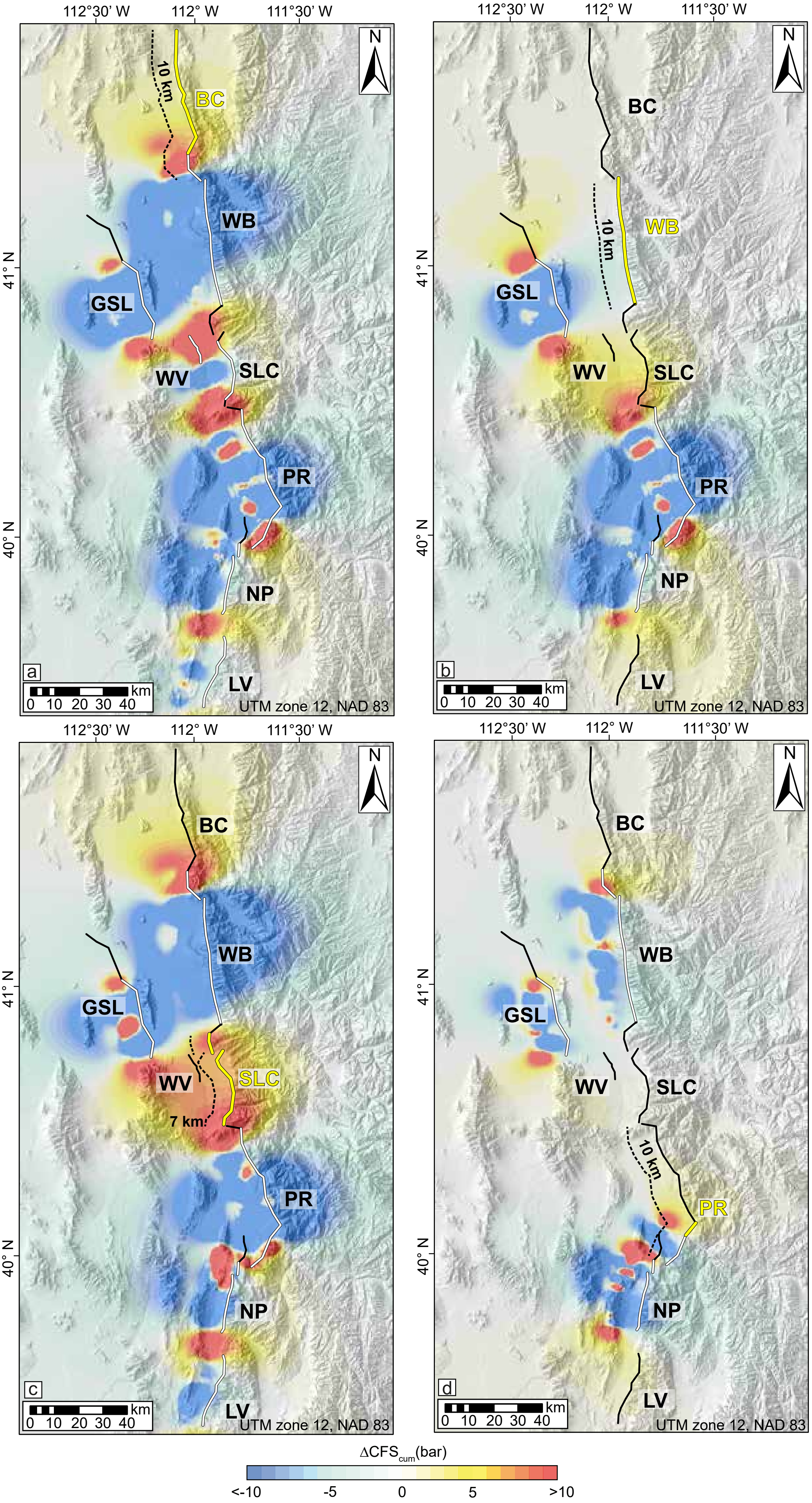

Figure 2. Cumulative (coseismic + postseismic) ΔCFS due to the earthquakes that have occurred since the most recent event of the receiver fault. Cumulative ΔCFS are calculated on the kinematics of (a) the Brigham City segment (BC), (b) the Weber segment (WB), (c) the Salt Lake City segment (SLC), (d) the southern part of the Provo segment (PR). Thick white lines are source faults; thick yellow lines are receiver faults; dashed black lines represent the depth-contour of the receiver fault at calculation depth where maximum ΔCFS are calculated. Refer to Table 2 for source earthquakes and receiver faults. NP=Nephi segment, LV=Levan segment, GSL=Great Salt Lake fault, WV=West Valley fault zone. National Elevation Dataset available from the U.S. Geological Survey.

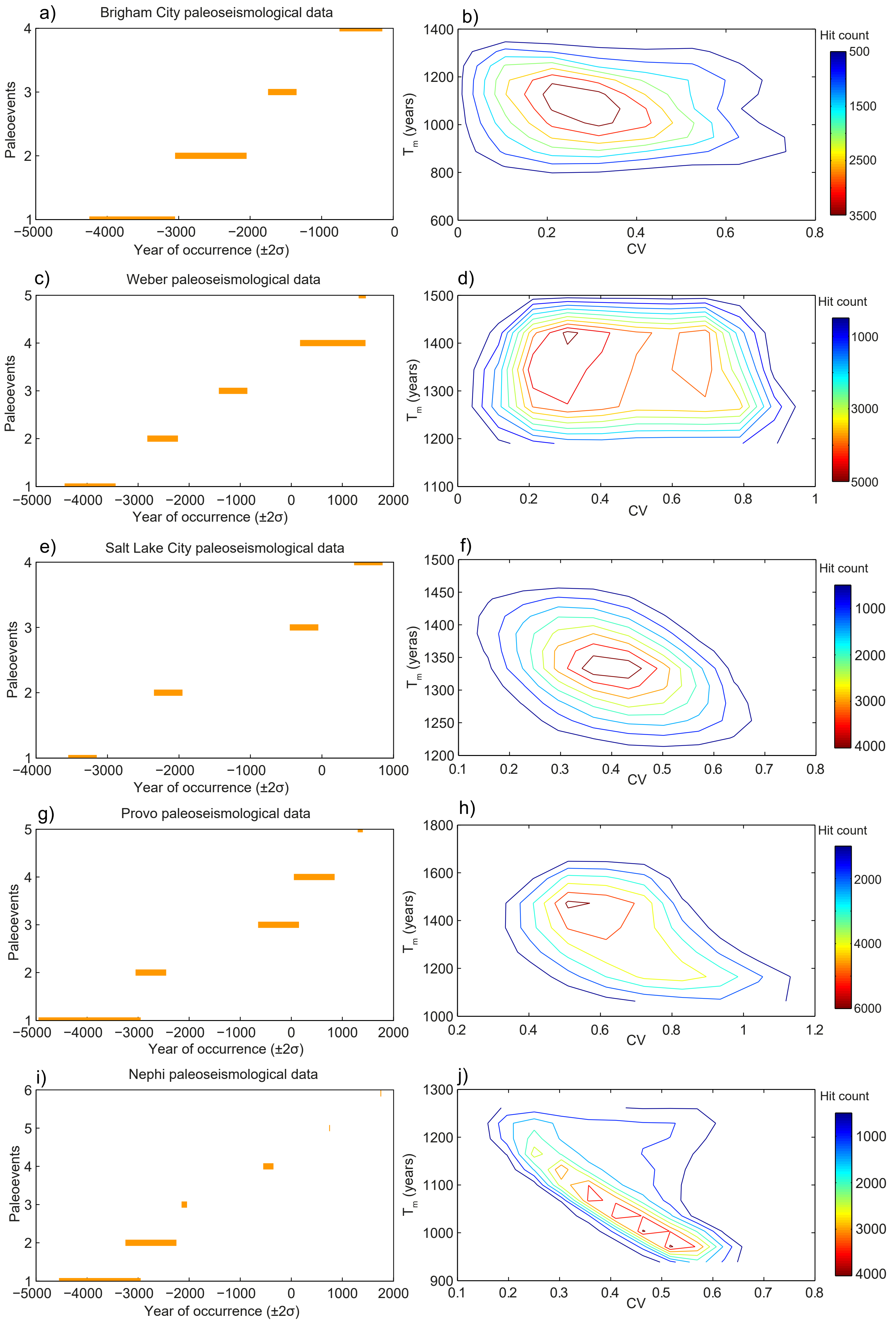

Figure 3. Paleoseismological data and results from the Monte Carlo simulations for (a, b) the Brigham City segment, (c, d) the Weber segment, (e, f) the Salt Lake City segment, (g, h) the Provo segment, and (i, j) the Nephi segment. T_m and CV are respectively the mean recurrence and the coefficient of variation.

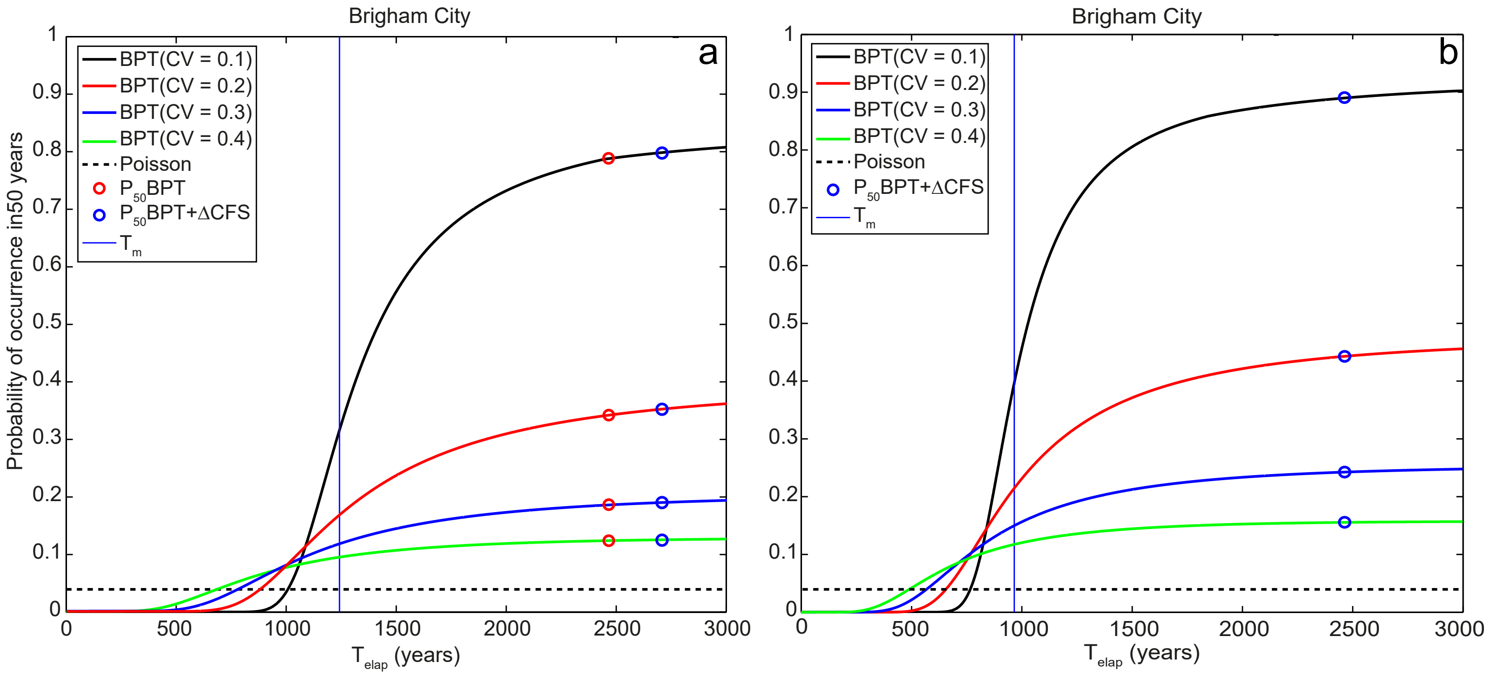

Figure 4. BPT probability curves calculated for the Brigham City segment for the next 50 years using different values of coefficient of variation (CV). Red circles represent the BPT probabilities when ΔCFS is not considered. Blue circles represent BPT probabilities when ΔCFS is considered using (a) the approach based on modified T_{elap}, and (b) the approach based on modified T_m. Dashed black line is the time-independent Poisson probability. T_{elap} and T_m are respectively the time elapsed since the most recent event, and the mean recurrence time.

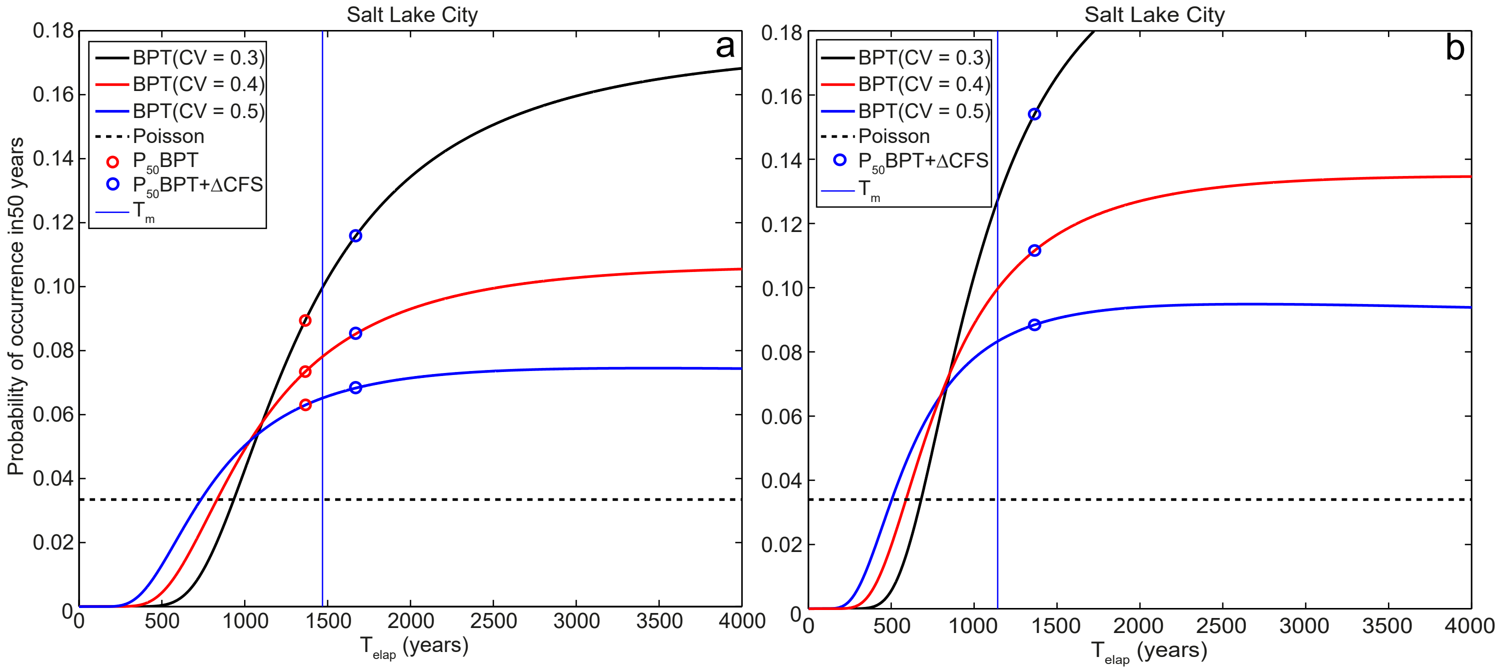

Figure 5. BPT probability curves calculated for the Salt Lake City segment for the next 50 years using different values of coefficient of variation (CV). Red circles represent the BPT probabilities when ΔCFS is not considered. Blue circles represent BPT probabilities when ΔCFS is considered using (a) the approach based on modified T_{elap}, and (b) the approach based on modified T_m. Dashed black line is the time-independent Poisson probability. T_{elap} and T_m are respectively the time elapsed since the most recent event, and the mean recurrence time.

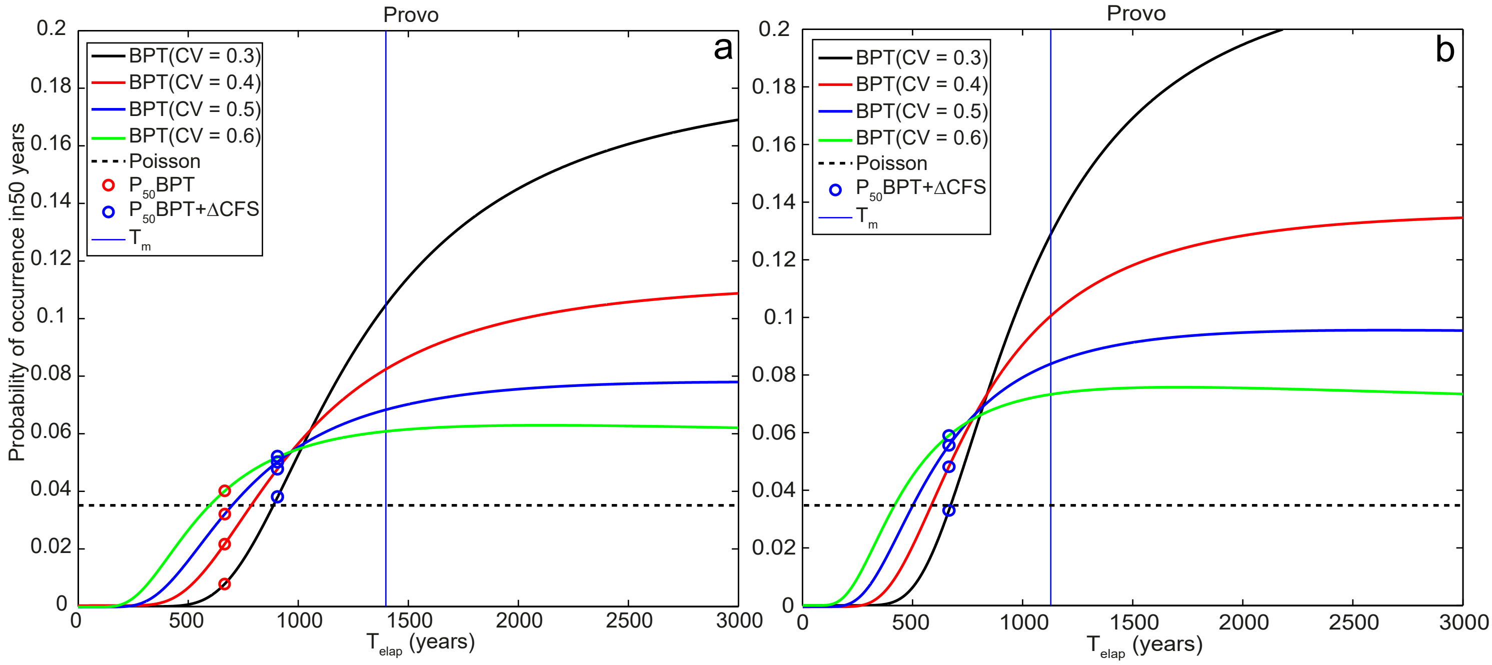

Figure 6. BPT probability curves calculated for the Provo segment for the next 50 years using different values of coefficient of variation (CV). Red circles represent the BPT probabilities when ΔCFS is not considered. Blue circles represent BPT probabilities when ΔCFS is considered using (a) the approach based on modified T_{elap}, and (b) the approach based on modified T_m. Dashed black line is the time-independent Poisson probability. T_{elap} and T_m are respectively the time elapsed since the most recent event, and the mean recurrence time.

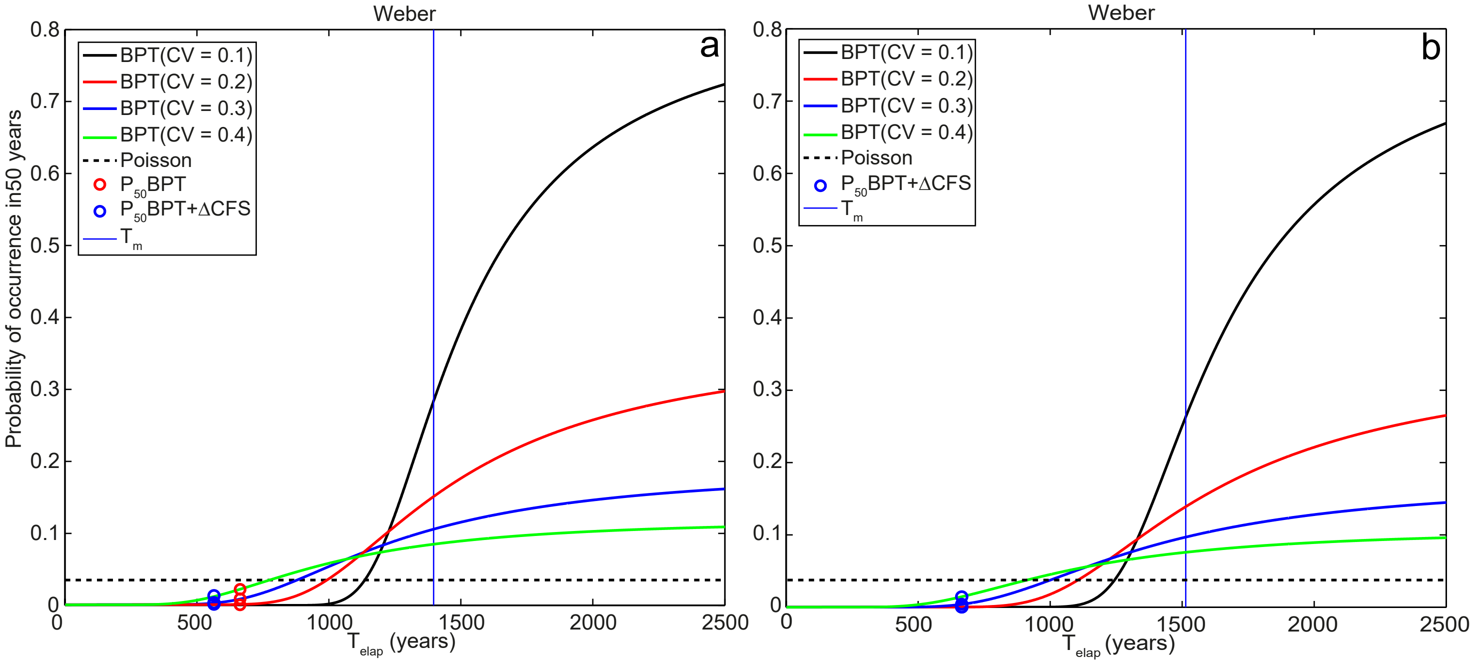

Figure 7. BPT probability curves calculated for the Weber segment for the next 50 years using different values of coefficient of variation (CV). Red circles represent the BPT probabilities when ΔCFS is not considered. Blue circles represent BPT probabilities when ΔCFS is considered using (a) the approach based on modified T_{elap}, and (b) the approach based on modified T_m. Dashed black line is the time-independent Poisson probability. T_{elap} and T_m are respectively the time elapsed since the most recent event, and the mean recurrence time.

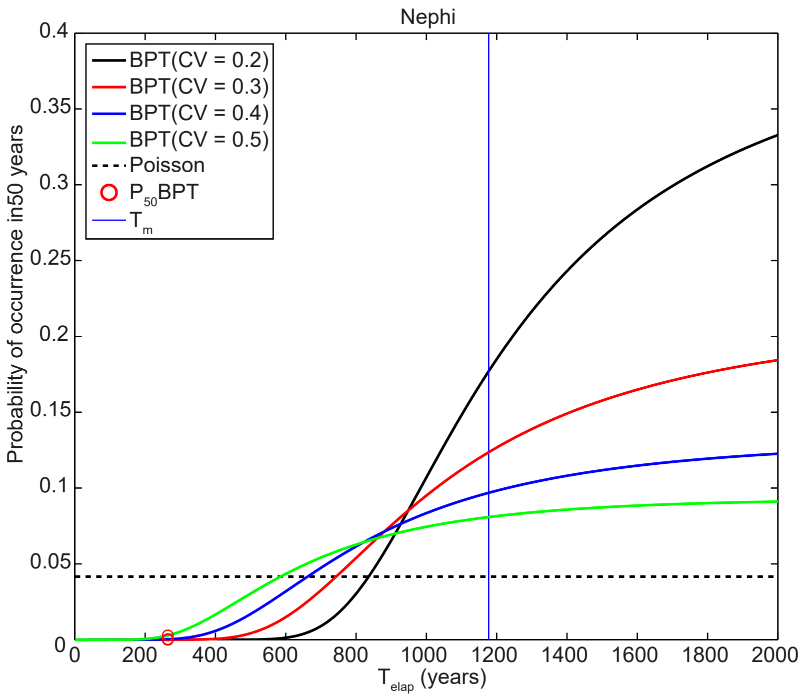

Figure 8. BPT probability curves calculated for the Nephi segment for the next 50 years using different values of coefficient of variation (CV). Red circles represent the BPT probabilities. Dashed black line is the time-independent Poisson probability. T_{elap} and T_m are respectively the time elapsed since the most recent event, and the mean recurrence time.

Table S1. Probability of a single-segment rupture for the next 50 years (P_{50}), calculated on each of the five main segment of the central WFZ using a lognormal probability distribution.

Segment	CV	P_{50}Poisson	P_{50}logn	P_{50}logn+ΔCFS_{cum} (T'_{elap})	P_{50}logn+ΔCFS_{cum} (T'_m)
Brigham City	0.1	3.9%	76.9%	78.1%	85.2%
	0.2		35.4%	35.6%	43.0%
	0.3		19.3%	19.2%	23.6%
	0.4		12.6%	12.5%	15.3%
Weber	0.1	3.5%	0.0%	0.0%	0.0%
	0.2		0.0%	0.0%	0.0%
	0.3		0.9%	0.2%	0.8%
	0.4		2.2%	1.1%	2.2%
Salt Lake City	0.3	3.3%	11.4%	13.9%	18.2%
	0.4		8.9%	10.0%	12.9%
	0.5		7.4%	7.9%	10.2%
Provo	0.3	3.5%	0.5%	2.9%	5.3%
	0.4		1.6%	4.0%	6.4%
	0.5		2.6%	4.4%	6.8%
	0.6		3.3%	4.6%	6.9%
Nephi	0.2	4.2%	0.0%	0.0%	0.0%
	0.3		0.0%	0.0%	0.0%
	0.4		0.1%	0.1%	0.1%
	0.5		0.6%	0.6%	0.6%

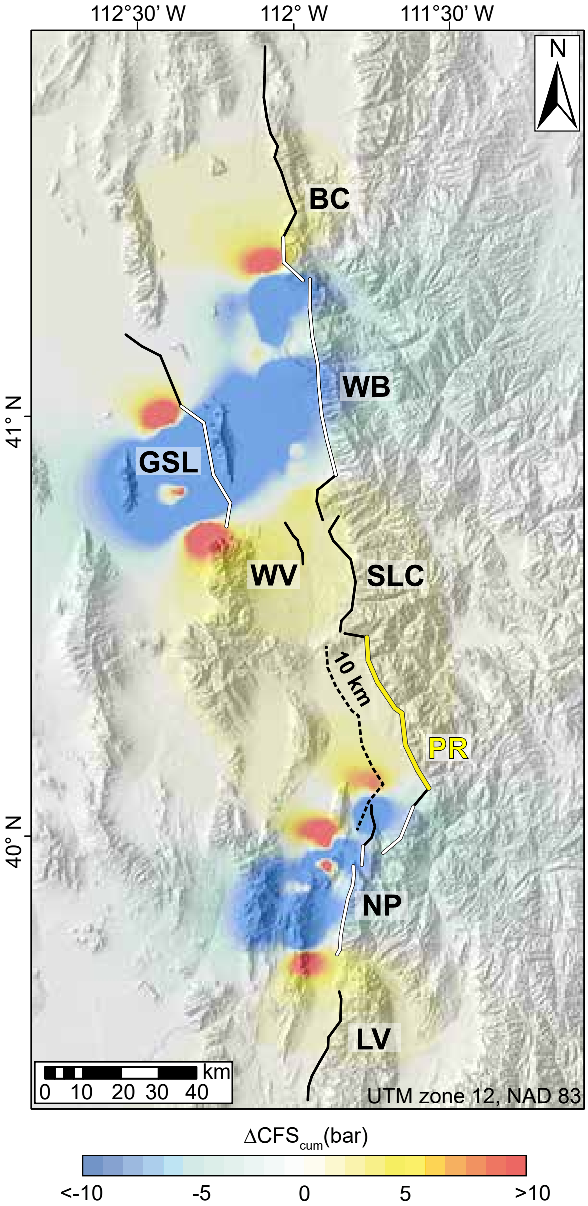

Figure S1. Cumulative (coseismic + postseismic) ∆CFS due to the earthquakes that have occurred since the most recent event of the Provo segment. Cumulative ∆CFS are calculated on the kinematics of the northern part of the Provo segment (PR). Thick white lines are source faults; thick yellow line is the receiver fault; dashed black line represents the depth-contour of the receiver fault at calculation depth. Refer to Table 2 for source earthquakes and receiver faults. NP=Nephi segment, LV=Levan segment, GSL=Great Salt Lake fault, WV=West Valley fault zone. National Elevation Dataset available from the U.S. Geological Survey.

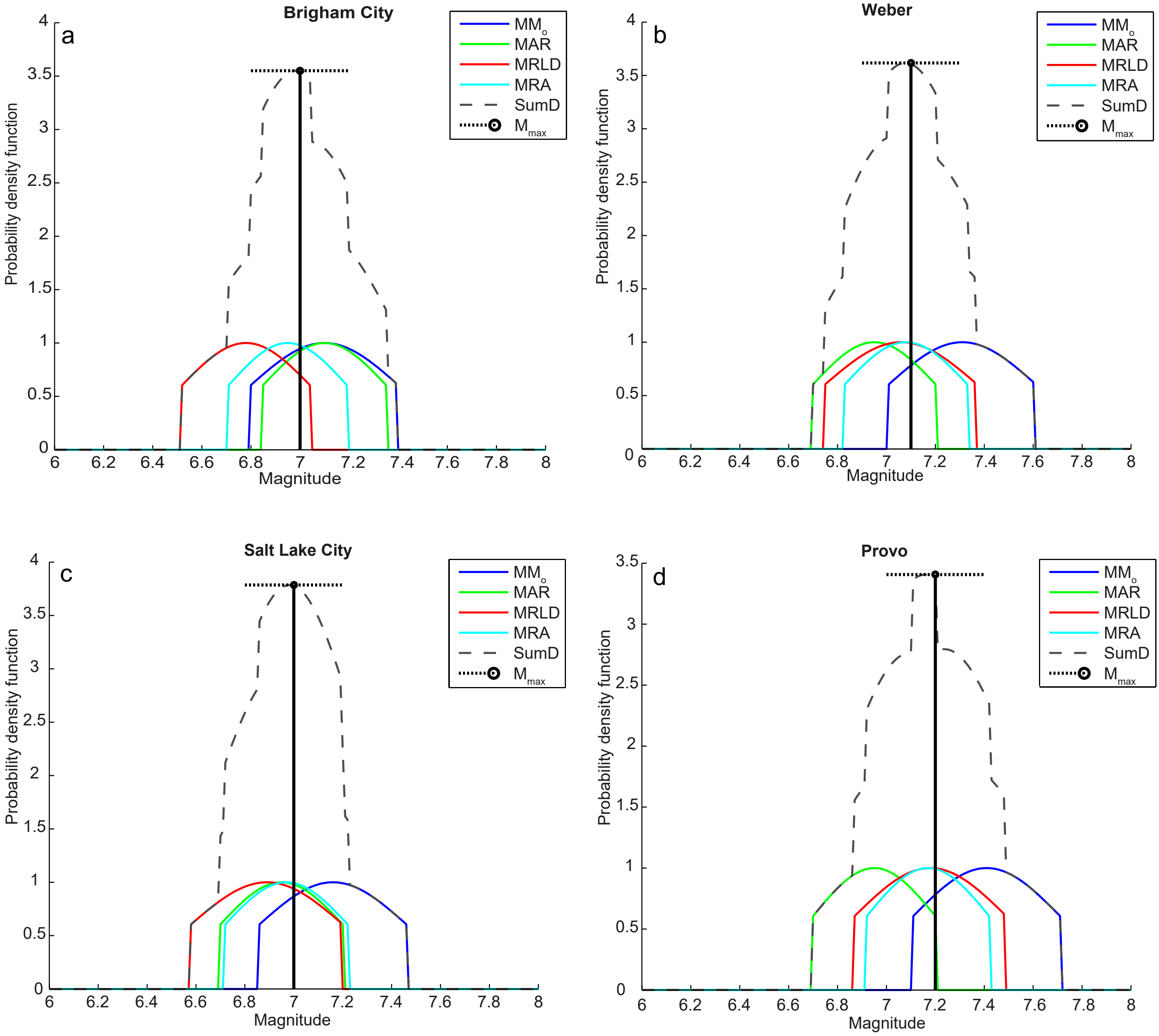

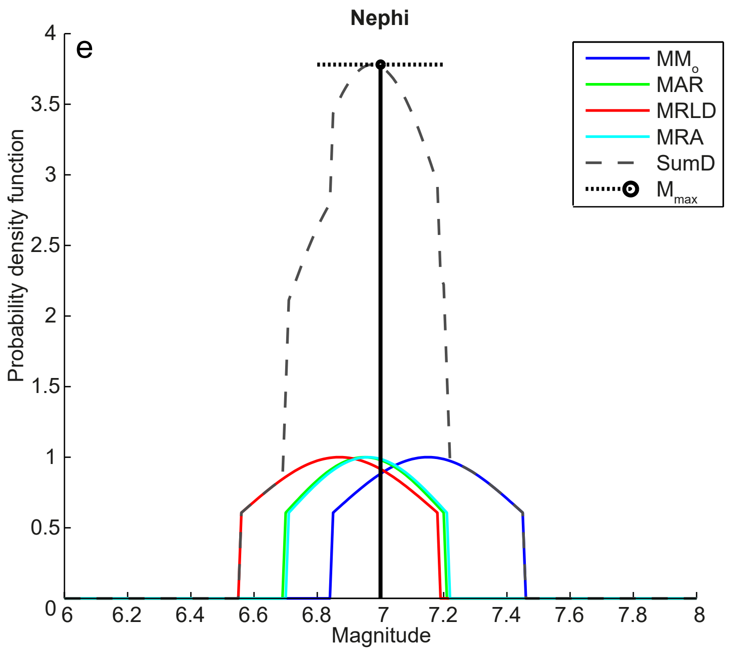

Figure S2. Magnitude distribution calculated for each of the five segments of the central WFZ. The dashed black line (SumD) represents the summation of the M_{max} values based on seismic moment (M_o), aspect ratio (AR), subsurface lenght (RLD), and rupture area (RA). The vertical black line represents the central value of the Gaussian fit of the summed probability density curves (M_{max}), and its standard deviation is given by the horizontal black dotted line.

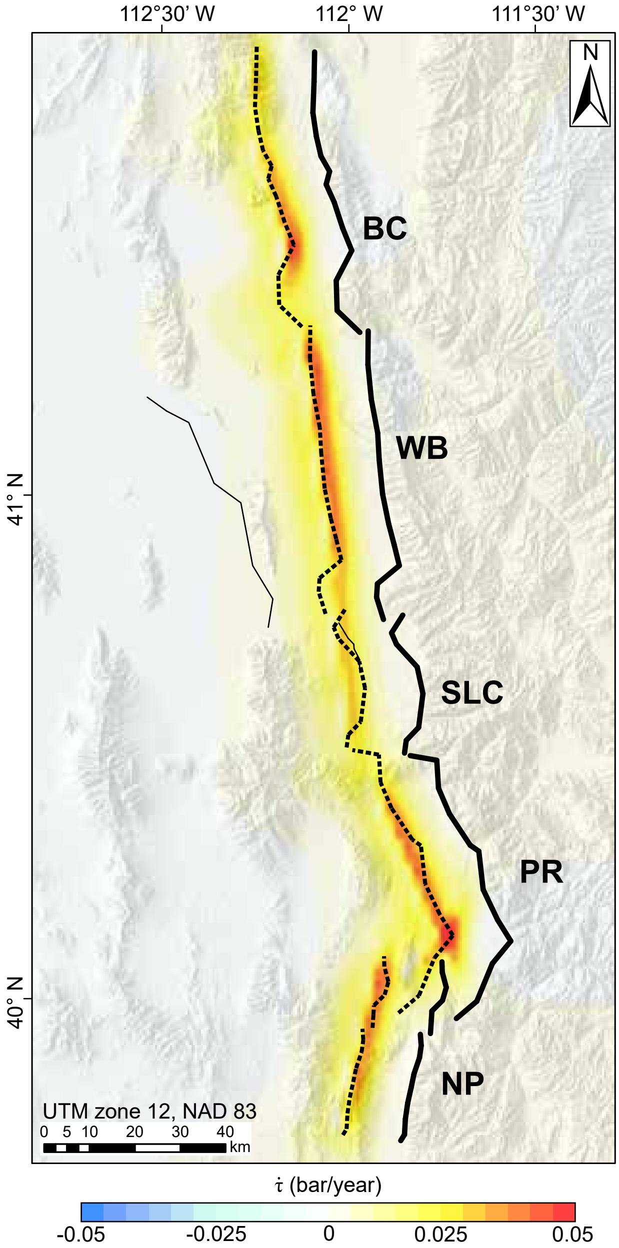

Figure S3. Tectonic loading ($\dot{\tau}$) calculated on the main orientation and kinematics (176˚ strike, 50˚ dip, and -90˚ rake) of the central WFZ at 13 km depth. Dashed black lines represent the 13 km contours of the central segments of the WFZ. BC=Brigham City segment, WB=Weber segment, SLC=Salt Lake City segment, PR=Provo segment, NP=Nephi segment. National Elevation Dataset available from the U.S. Geological Survey.